

Elemental Geochemistry of Sedimentary Rocks in Yellowknife Bay, Gale Crater, Mars

Scott M. McLennan^{1,*}, R. B. Anderson², J. F. Bell III³, J. C. Bridges⁴, F. Calef III⁵, J. L. Campbell⁶, B. C. Clark⁷, S. Clegg⁸, P. Conrad⁹, A. Cousin⁸, D. J. Des Marais¹⁰, G. Dromart¹¹, M. D. Dyar¹², L. A. Edgar³, B. L. Ehlmann^{5,13}, C. Fabre¹⁴, O. Forni¹⁵, O. Gasnault¹⁵, R. Gellert⁶, S. Gordon¹⁶, J. A. Grant¹⁷, J. P. Grotzinger¹³, S. Gupta¹⁸, K. E. Herkenhoff², J. A. Hurowitz¹, P. L. King¹⁹, S. Le Mouélic²⁰, L. A. Leshin²¹, R. Lévillé²², K. W. Lewis²³, N. Mangold²⁰, S. Maurice²⁴, D. W. Ming²⁵, R. V. Morris²⁵, M. Nachon²⁰, H. E. Newsom¹⁶, A. M. Ollila¹⁶, G. M. Perrett⁶, M. S. Rice¹³, M. E. Schmidt²⁶, S. P. Schwenzer²⁷, K. Stack¹³, E. M. Stolper¹³, D. Y. Sumner²⁸, A. H. Treiman²⁹, S. van Bommel⁶, D. T. Vaniman³⁰, A. Vasavada⁵, R. C. Wiens³¹, R. A. Yingst³⁰

Affiliations:

¹ Department of Geosciences, State University of New York at Stony Brook, Stony Brook, NY, 11794-2100, USA.

² U.S. Geological Survey, Astrogeology Science Center, Flagstaff, AZ 86001, USA.

³ School of Earth and Space Exploration, Arizona State University, Tempe, AZ 85287, USA

⁴ Space Research Centre, Dept. of Physics & Astronomy, University of Leicester LE1 7RH, UK

⁵ Jet Propulsion Laboratory, California Institute of Technology, Pasadena, CA 91109, USA.

⁶ Department of Physics, University of Guelph, Guelph, ON, N1G 2W1, Canada

⁷ Space Science Institute, Boulder, CO, USA

⁸ Chemistry Division, Los Alamos National Laboratory, Los Alamos, NM, 87545, USA

⁹ NASA Goddard Space Flight Center, Greenbelt, MD 20771, USA.

¹⁰ Department of Space Sciences, NASA Ames Research Center, Moffett Field, CA 91109, USA.

¹¹ Laboratoire de Géologie de Lyon, Université de Lyon, 69364 Lyon, France.

¹² Department of Astronomy, Mt Holyoke College, South Hadley, MA 01075, USA.

¹³ Division of Geological and Planetary Sciences, California Institute of Technology, Pasadena, CA 91125, USA

¹⁴ UMR 7359 CNRS-Georesources, Campus des Aiguillettes, Faculté des Sciences, BP 70239, 54506 Vandoeuvre Les Nancy, Cedex, France.

¹⁵ IRAP, 9, avenue du Colonel Roche, BP 44346, 31028 Toulouse, Cedex 4, France.

¹⁶ Institute of Meteoritics, University of New Mexico, Albuquerque, NM 87131, USA.

¹⁷ Center for Earth and Planetary Sciences, National Air and Space Museum, Smithsonian Institution, 6th at Independence SW, Washington, DC 20560, USA.

¹⁸ Department of Earth Science and Engineering, Imperial College London, London, SW7 2AZ, UK.

¹⁹ Research School of Earth Sciences, Australian National University, Canberra, ACT, 0200, Australia.

²⁰ Laboratoire de Planétologie et Géodynamique, LPGN/CNRS UMR 6112 and Université de Nantes, 4432 Nantes, France

²¹ School of Science, Rensselaer Polytechnic Institute, Troy, NY 12180, USA.

²² Canadian Space Agency, St-Hubert, QC, J3Y 8Y9, Canada.

²³ Princeton University, Princeton, NJ 08544, USA.

²⁴ Observatoire Midi-Pyrenees, Toulouse, France.

²⁵ NASA Johnson Space Center, Houston, TX 77058, USA.

²⁶ Department of Earth Sciences, Brock University, St. Catharines, ON L2S 3A1, Canada.

²⁷ CEPSAR, Open University, Milton Keynes MK7 6AA, U.K.

²⁸ Geology Department, University of California, Davis, CA 95616, USA.

²⁹ Lunar Planetary Science Institute, Houston, TX 77058, USA

³⁰ Planetary Science Institute, Tucson, AZ, 85719, USA

³¹ International Space and Response Division, Los Alamos National Laboratory, Los Alamos, NM, 87545, USA.

*Correspondence to: Scott.McLennan@stonybrook.edu

Abstract: The source for Yellowknife Bay fluvio-lacustrine sedimentary rocks was Fe-rich basalts that evolved from a composition similar to average Mars crust to one strongly influenced by alkaline basalts. Mudstones at the base preserve slight stratigraphic provenance variations and may contain minor (<4%) meteoritic components. Major elements preserve no evidence of chemical weathering indicating arid, possibly cold, paleoclimates and rapid erosion/deposition. Absence of predicted geochemical variations indicates that magnetite and phyllosilicates identified in Yellowknife Bay formation mudstones formed by diagenesis under low temperature, circum-neutral pH, rock-dominated aqueous conditions. High spatial resolution analyses of diagenetic features (concretions, raised ridges, fractures) indicate they are composed of Fe-Cl-Br-Ni-Ge-rich components, variably hydrated Ca-sulfates and Fe-Mg-Cl rich components, respectively, and the composition of a cross-cutting dike-like feature is consistent with a sedimentary intrusion. The geochemistry of the Yellowknife Bay formation provides further evidence for diverse depositional and diagenetic sedimentary environments during the early history of Mars.

One Sentence Summary: Chemical compositions of fluvio-lacustrine clastic sedimentary rocks in Gale crater, Mars, demonstrate evolving sources and a multistage diagenetic aqueous fluid history.

Introduction: Shortly after leaving its landing site at Bradbury Landing in Gale crater, the Mars Science Laboratory *Curiosity* rover traversed to Yellowknife Bay (1), where it encountered a flat-lying, ~4.75 meter thick succession of weakly-indurated clastic sedimentary rocks ranging from mudstones at the base to mainly sandstones at the top (2). Stratigraphic relationships and sedimentary structures indicate that this coarsening-upward succession likely represents sedimentation in an ancient fluvio-lacustrine system that would have been habitable. Also preserved is a spectrum of diagenetic features, including concretions, void spaces with a variety of sizes, geometries and origins, early diagenetic fractures (“raised ridges”) filled with banded (possibly silicate) cements, possible sedimentary dikes, and a later diagenetic fracture system filled with sulfate cements, all indicating extended post-depositional aqueous fluid flow through the rocks (2).

Curiosity fully applied its analytical payload to investigate these sedimentary rocks and determine lithological, textural, chemical, mineralogical and isotopic compositions and their stratigraphic relationships (2-4). The payload of *Curiosity* includes two instruments capable of measuring elemental abundances. The alpha particle X-ray spectrometer (APXS) determines abundances on ~2.25 cm² surfaces and when used in conjunction with the dust removal tool (DRT) or drilling system, can analyze relatively clean surfaces and drill cuttings. The laser-induced breakdown spectrometer (LIBS), part of the ChemCam remote sensing suite, detects atomic emission spectra from areas of ~0.1-0.3 mm² (depending on standoff distance), >2 orders of magnitude smaller than APXS. LIBS offers the additional capability of laser depth profiling (including surface dust removal) of up to ~1000 μm. These instruments provide complementary data by revealing both bulk rock compositions and compositions that can be related directly to textural features.

On Earth, the elemental geochemistry of clastic sedimentary rocks provides information central to interpreting sedimentary history, including chemical weathering history, nature and composition of the sediment provenance, sediment transport, and diagenetic history (5-10). In turn, geochemical understanding of these issues constrains many fundamental geological questions such as paleoclimates, tectonic relationships, basin evolution, diagenetic fluid flow and even crust-mantle evolution (7,11-15). Experience from the Mars Exploration Rovers *Spirit* and *Opportunity* and from orbital spectroscopy further shows that such approaches are applicable to sedimentary environments on Mars (12,16-22). Accordingly, the purpose of this paper is to report elemental geochemistry of the ancient sedimentary rock succession, including its diagenetic features, preserved within Yellowknife Bay, evaluate these compositions in terms of the sedimentary history of this habitable paleoenvironment within Gale crater and place them within the context of Martian surface environments early in the planet’s history.

Yellowknife Bay Stratigraphy: The geology, stratigraphy, sedimentology and diagenetic history of Yellowknife Bay are described by *Grotzinger et al.* (2). The sedimentary sequence, informally named the Yellowknife Bay formation, is subdivided into four members (Fig. 1) that likely were deposited in a prograding alluvial fan fluvio – lacustrine depositional system and influenced by at least two distinct diagenetic events. The formation is likely Hesperian in age but poorly constrained and could lie anywhere between early Hesperian (~3.7-3.4 Ga), if part of the early Gale crater fill, to late Hesperian or early Amazonian (~3.4-1.5 Ga), if coeval with the nearby Peace Vallis alluvial fan exposed in Gale crater (2).

The stratigraphically lowest Sheepbed member (>1.5 meter thick), whose base is not exposed, is composed of drab-colored, bedded mudstone. Fine-grained texture, laterally extensive decimeter-scale bedding and stratigraphic relationships indicate deposition from suspension, likely in a distal alluvial fan lacustrine environment but possibly as ash fall. Early diagenetic textures include millimeter-scale nodules interpreted as concretions, millimeter-scale rimmed “minibowls” interpreted as void space possibly formed by gas expulsion during early diagenesis, and narrow centimeter-sized intersecting “raised ridges”, laterally correlative to nodules and minibowls, possessing resistant isopachous cements lining ridge margins, and interpreted as diagenetic cracks formed in early lithified sediment probably by reactions involving pore fluids (see Figs. 6A-C, 7 in ref. 2). The upper ~50-75 centimeters of the Sheepbed member weathers more recessively than underlying beds and possesses higher abundances of both early and late diagenetic features. For geochemistry, we further subdivided the Sheepbed member into lower and upper parts with the boundary ~30 centimeters beneath the Gillespie Lake member in order to evaluate compositional transitions into the overlying stratigraphic unit.

The ~1.1 meter thick Gillespie Lake member overlies the Sheepbed member with a sharp, likely erosional, contact. It consists of thin to medium bedded medium- to very coarse-grained sandstones with relict centimeter-scale cross-bedding. Mars Hand Lens Imager (MAHLI) and ChemCam Remote Micro-Imager (RMI) images indicate textural immaturity and compositionally diverse grains (see Fig. 5D in ref. 2). This member was likely deposited in a distal fluvial environment. Gillespie Lake sandstones exhibit little primary porosity, suggesting a cemented rock, but contain secondary porosity in the form of dispersed millimeter-scale vugs. The Sheepbed (including early diagenetic features) and Gillespie Lake members are both cross-cut by a network of later diagenetic (post-lithification) intersecting fractures of variable thickness (hairline to ~8 millimeters) filled with light-toned cement, identified as Ca-sulfate by a variety of measurements (see below). These filled fractures are most abundant within the uppermost Sheepbed and the bright cements also fill minibowls where they intersect with fractures. Also cross-cutting the upper Sheepbed member is a ~8 centimeter wide dike-like feature termed the “snake”, that terminates in a small anticline within the middle Gillespie Lake member, and is interpreted as a sedimentary dike injected due to high pore pressures that developed during rapid burial (2). A detailed 1.5 meter stratigraphic section, termed the Selwyn Section, was measured across the Sheepbed – Gillespie Lake contact and serves effectively as a type section (Fig. 1, Supplemental Fig. S1).

The two upper members are less clearly laterally continuous (2). The Point Lake member (~0.4 meters) is poorly understood but notable in possessing abundant millimeter- to centimeter-scaled vugs. Possible interpretations include a debris flow, volcanoclastic layer, gas-charged sedimentary sill, perhaps related to the “snake”, or a vesicle-rich volcanic flow although there is no evidence for a nearby contemporaneous volcanic source. Some vugs and cross-cutting fractures are filled with light-toned minerals, identified as Ca-sulfate by ChemCam, reminiscent of fracture fillings in the Sheepbed and Gillespie Lake members. In this paper, we assume the Point Lake member is sedimentary but are mindful of this uncertainty. The heterogeneous Shaler member (~1.7 meters) consists of commonly cross-bedded interstratified sandstones and recessive finer-grained sediment and was likely deposited mainly by fluvial processes, with paleocurrents indicating a source derived from the direction of the crater rim. Within this member are discontinuous fine-grained beds, in some cases with distinctive chemical compositions and possibly with distinctive origins (see below).

Mineralogical and Geochemical Constraints from CheMin and SAM: Two locations within the upper Sheepbed member, corresponding to APXS targets John_Klein and Cumberland, were drilled with recovered powders being sieved (<150 μm) and delivered to CheMin and SAM for X-ray diffraction analysis of mineralogy and chemical - isotopic measurements of evolved gases using gas chromatography, quadrupole mass spectrometry and tunable laser spectrometry (3,4). Unsurprisingly for clastic sediments, both samples are composed of non-equilibrium mineral assemblages including primary igneous and a variety of secondary phases, notable for a ~30-40% amorphous component (including allophane-like material) and ~20% trioctahedral phyllosilicates consisting of a ~10Å collapsed saponitic smectite in John_Klein and clay minerals in Cumberland with both ~13.2Å and ~10Å spacing, possibly reflecting different cations or metal-hydroxyl groups filling interlayer spacing. The remaining crystalline mineralogy includes (in decreasing amount) plagioclase, pyroxene, magnetite, Ca-sulfate (anhydrite, bassanite), forsteritic olivine (John_Klein only), akaganeite, sanidine, pyrrhotite and possibly (<1-2%) hematite, ilmenite, pyrite, quartz and halite. SAM analyses are also consistent with smectite, sulfates, sulfides, Fe-oxides and further indicate oxychlorine compounds (e.g., chlorate and/or perchlorate). Both instruments indicate heterogeneous Fe- and S-redox states. Mass balance calculations provide estimates of the chemical compositions of the combined amorphous component plus phyllosilicates and remaining crystalline minerals and these compositions (4) are used below.

Analyses and Data: APXS is a well-established analytical technique on Mars, providing quantitative abundance data for major and minor elements, including S and Cl, and trace elements Cr, Ni, Zn, Ge and Br (23). Analytical details are provided in the [Supplemental Information \(APXS Methods\)](#) and Yellowknife Bay formation results are provided in [Supplemental Tables S1-S3](#). Multiple APXS analyses were sometimes obtained on the same rock but at different locations. In some cases (e.g., Bathurst Inlet) both analyses are considered because they represent slightly different stratigraphic levels. However, where multiple analyses were made at a single site, such as drill sites (e.g., John_Klein, Cumberland) and APXS “rasters” (e.g., Sayunei, McGrath), the analysis with lowest SO_3 was selected as most representative of the sedimentary rock since brushed surfaces indicate low SO_3 and mapping of borehole walls suggests Ca-sulfate abundances correlate with diagenetic light-toned veins and minibowl fills. APXS

“rasters”, involving multiple, closely spaced measurements, were employed on two diagenetic features: fracture fills (Sayunei) and raised ridges (McGrath) and these results are provided in [Supplemental Table S4](#), which also includes the suggested sedimentary dike (Snake_River analysis). The ChemCam LIBS instrument provides semi-quantitative analyses for major and some minor and trace elements (e.g., Ba, Rb, Sr, Li) using multiple laser pulses (shots) on ~350-550 μm diameter targets from up to 7 meters distance (24,25). The first ~5 shots remove surface dust and the rock analyses are based on averages of subsequent shots. Analytical details are provided in the [Supplemental Information \(ChemCam Methods\)](#).

Clastic Sedimentary Rocks: Yellowknife Bay S- and Cl-free compositions (all on weight percent basis) determined by APXS correspond to iron-rich basalt (i.e., SiO_2 mostly <48%; FeO_T mostly >20%; $\text{MgO} \approx 8\text{-}10\%$; $\text{Ni} \approx 200\text{-}900\text{ppm}$). Alkalis are variable ($\text{Na}_2\text{O}+\text{K}_2\text{O} \approx 3\text{-}6\%$; $\text{K}_2\text{O}/\text{Na}_2\text{O} \approx 0.2\text{-}1.3$). CaO is highly variable ($\approx 5\text{-}25\%$) but values above ~7% correspond to high SO_3 , indicative of elevated levels of Ca-sulfate. Typical for the Martian surface, both SO_3 and Cl are mostly elevated in APXS observations due in part to surface soil and dust contamination. On brushed surfaces, APXS measurements of SO_3 are as low as 0.9% (Werneke_Brush) suggesting the sedimentary rocks may have no more than 1-2% SO_3 on average. On the other hand, Cl abundances are higher than in most Martian soils (26), reaching 1.9% and commonly leading to low S/Cl ratios. Elevated Cl abundances ($\geq 1\%$) are likely a primary rock feature rather than resulting from soil/dust coatings, consistent with the presence of oxychlorine compounds, akaganeite and possibly halite (3,4). Up to 9% magnetite in the crystalline component of Sheepbed mudstone drill samples was detected by XRD (4). Bulk rock geochemistry suggests this is not detrital; for example there are no systematic relationships between FeO_T/MgO and FeO_T that could be explained by magnetite variations, no correlations with elements that might form part of a heavy mineral suite (e.g., Cr, Ti) and no geochemical evidence for detrital magnetite enrichments (e.g., Fe-enrichment) in immediately overlying Gillespie Lake sandstones where heavy minerals might be expected to concentrate even more. Absence of geochemical evidence for detrital magnetite is also consistent with deposition of the Sheepbed mudstones from suspension into a lake, where heavy mineral concentrations are highly unlikely (2,4). Accordingly, we conclude that magnetite is most likely a diagenetic phase rather than a detrital component.

Geochemical relationships are well illustrated in ternary diagrams plotting mole fractions $\text{Al}_2\text{O}_3 - (\text{CaO}+\text{Na}_2\text{O}) - \text{K}_2\text{O}$ (or A-CN-K) and $\text{Al}_2\text{O}_3 - (\text{CaO}+\text{Na}_2\text{O}+\text{K}_2\text{O}) - (\text{FeO}_T+\text{MgO})$ (or A-CNK-FM) (Fig. 2). On these diagrams igneous minerals plot on or below the plagioclase - K-feldspar (A-CN-K) and feldspar - FM (A-CNK-FM) joins whereas secondary clay minerals plot above (29). The Chemical Index of Alteration (CIA), defined as $100 \cdot \text{A}/(\text{A}+\text{C}+\text{N}+\text{K})$, reveals any chemical weathering history by quantifying the systematic loss of relatively mobile elements, and the scale is plotted beside the A-CN-K diagrams. For mafic sources, CIA above ~40-45 in bulk sediment suggests some chemical weathering history and above ~50-55 provides fairly compelling evidence for open system weathering (10). ChemCam (Fig. 2C, D) analyzed many more targets than APXS (Fig. 2A, B), and given the strategy of using its greater spatial resolution to target textural features (e.g., veins, ridges, grains), more scatter is both

expected and observed. Mission experience so far indicates a slight instrument bias with ChemCam data plotting at higher Al_2O_3 and lower Na_2O and K_2O on these diagrams than APXS, especially for alkali-rich compositions, and this is the subject of ongoing calibration efforts. Nevertheless, the analyses provide consistent geochemical trends.

Lower Sheepbed and Gillespie Lake bulk rock compositions (Fig. 2A,B) are tightly grouped, and slightly more mafic than average Martian crust (closer to FM apex). Most upper Sheepbed samples plot in a similar position but several trend towards the CN and CNK apexes, where Ca-sulfate plots. ChemCam analyses (Fig. 2C, D) show a more complete linear trend, with one end member defined by Ca-sulfates within the light-toned fractures and filled minibowls that were targeted for analysis. Point Lake and Shaler members have bulk compositions that commonly differ from both average crust and Sheepbed/Gillespie Lake, with less relative amounts of $\text{FeO}_T + \text{MgO}$ and higher K_2O in some samples, characteristics confirmed by ChemCam analyses that also show evidence for detrital feldspar (Fig. 2D). Schmidt *et al.* (30) evaluated the first four rocks analyzed by APXS, including Yellowknife Bay formation samples Bathurst Inlet and Rocknest3, as well as the out of place rocks Jake_Matijevic and Et Then interpreted to be volcanoclastic or igneous. Elemental relationships among these rocks are consistent with physical mixing between Bathurst Inlet-like and Jake_Matijevic-like material (30). Some ChemCam analyses plot above the plagioclase – K-feldspar and feldspar – FM joins suggesting phyllosilicate-rich targets, consistent with the identification of phyllosilicates by XRD (4). In addition, some ChemCam Sheepbed analyses plot closer to the FM apex, consistent with the identification of Mg-Fe-Cl-rich phases associated with raised ridges (also observed in the McGrath APXS raster) that were also targeted for analysis (see below) and the Fe^{3+} -rich phases identified by XRD (e.g., magnetite, akaganeite, hematite).

Despite identifying phyllosilicates in Sheepbed mudstones by XRD (4) and inferring them from ChemCam (Fig. 2C,D), the geochemistry of the Yellowknife Bay formation provides scant support for any significant chemical weathering history affecting the sources or the sediment during transport into the depositional basin. During circum-neutral pH weathering, clay minerals form at the expense of primary igneous phases, with loss of mobile elements. As a result, bulk sedimentary rock compositions that have been influenced by weathering, including those derived from mafic sources, typically plot above the plagioclase – K-feldspar and feldspar – FM joins (31-33). Similarly, any clay minerals that formed by hydrothermal alteration (e.g., impact-related) in surrounding regions and transported into the Yellowknife basin would also carry comparable distinct chemical signatures (22,34-36). Nor is any evidence observed for low pH alteration conditions, in the form of Fe^{3+} mobility and associated formation of Fe^{3+} -sulfates, such as that observed by the *Spirit* and *Opportunity* rovers (37-39). During transport clays concentrate in fine-grained sediment (i.e., Sheepbed) compared to associated coarse-grained sediment (i.e., Gillespie Lake) but no evidence for the predicted geochemical fractionation related to hydraulic segregation of sediment types (including clay minerals and magnetite) is observed in the bulk analyses of either unit. Sheepbed mudstones exhibit no fissility as is commonly observed in fine-grained sediments consisting of transported clay minerals (40). One complicating factor is that secondary Ca-sulfate might lower apparent CIA values and mask evidence for chemical weathering. However, on a plot of CIA versus SO_3 content (Fig. 3), this clearly is not the

case. At high SO_3 , indicative of sulfates, CIA falls to lower values as expected but at lower SO_3 , CIA levels off to values typical of Martian mafic igneous rocks thus indicating that none of these samples has witnessed a significant chemical weathering history. This is also consistent with sample positions on the A-CNK-FM diagram (Fig. 2B). Accordingly, formation of phyllosilicates within Sheepbed mudstones likely resulted from diagenetic processes that did not noticeably influence bulk rock composition, implying rock-dominated (i.e., low water/rock ratio) aqueous fluid conditions.

Both major and trace elements exhibit stratigraphic trends. To avoid variations in absolute abundances imparted by simple dilution effects of Ca-sulfate, we plot ratios among elements most often associated with siliciclastic components. On a plot of $\text{K}_2\text{O}/\text{Al}_2\text{O}_3$ versus $\text{Al}_2\text{O}_3/\text{TiO}_2$ (Fig. 4A) Point Lake and Shaler members include samples with higher $\text{K}_2\text{O}/\text{Al}_2\text{O}_3$ and generally have more variable $\text{Al}_2\text{O}_3/\text{TiO}_2$, compared to the Sheepbed and Gillespie Lake members. The two analyses from the rock Bathurst Inlet, from near the top of the Shaler member, are especially distinctive in having the highest $\text{K}_2\text{O}/\text{Al}_2\text{O}_3$ ratios. These differences are interpreted to represent a significant change in the provenance from which sediment particles were derived to include more alkali-rich basalts higher in the stratigraphic section.

Subtle differences in bulk composition also exist within the Sheepbed member itself, with the upper part having slightly higher and more variable $\text{Al}_2\text{O}_3/\text{TiO}_2$ ($x=9.68$, $s.d.=0.96$) than the lower part ($x=8.63$, $s.d.=0.43$). This is also likely a provenance effect (41,42), although relationships between $\text{Al}_2\text{O}_3/\text{TiO}_2$ ratio and overall bulk composition is complex in detail, especially since all compositions are basaltic (12,43).

Stratigraphic variations in APXS trace elements are summarized on a plot of Cr/Ni versus Zn/Ni (Fig. 4B). In this case, the Point Lake and Shaler members have higher and/or more variable ratios than the Sheepbed member, related to combinations of elevated Zn and Cr and lower Ni. There may also be a difference between Gillespie Lake sandstones and Sheepbed mudstones, related mainly to lower Ni in the former, although only a single high quality analysis is available for the Gillespie Lake member. Major elements indicate a similar provenance and so the reason for this is not clear. A heavy mineral effect is one possibility but would be more likely to cause an enrichment of Cr (chromite) rather than depletion of Ni in the sandstones. Thus, in Shaler sandstones, Ni is similarly low (~200 ppm) as in the Gillespie Lake sandstone sample but Cr reaches very high levels (>5,000 ppm) consistent with a heavy mineral (chromite) enrichment predicted by fluvial processing (44). Within the Sheepbed member, the upper part has lower Cr/Ni and Zn/Ni, related mainly to higher Ni, consistent with a slightly different mafic provenance.

Lithium contents measured by ChemCam also reveal a stratigraphic trend (Fig. 4C) with Sheepbed mudstones having low and uniform abundances ($x=4.3$ ppm; $s.d.=2.4$ ppm) whereas the overlying units have about a factor of two higher and much more variable Li abundances. Although secondary aqueous processes, such as hydrothermal activity, can enrich Li (45) and evidence for centimeter-scale Li redistribution is observed in diagenetic raised ridges (see below), this range for average values probably cannot be distinguished from variations in basaltic provenance given our limited understanding of Li distributions in the Martian crust-mantle system.

Early Diagenetic Features: Efforts were made to characterize chemical and mineralogical controls on concretion formation within the Sheepbed member. Numerous ChemCam observations were directed at concretions but no systematic differences were observed, limiting compositional differences between concretion and host sediment to less than ~10% for major elements. APXS analyses of drill fines from concretion+minibowl-rich (Cumberland) and concretion+minibowl-poor (John_Klein) areas were also examined ([Supplemental Material - Mass Balance Calculations; Supplemental Table S6](#)). Samples delivered to the internal instruments (Chemin and SAM) that determined mineralogy (3,4) would be preferable but at the time of writing, *Curiosity* was still carrying the Cumberland sample and consequently it has not been analyzed by APXS. Additional complexity is that imaging of drill hole walls indicates John_Klein has greater amounts of Ca-sulfate-filled fractures (see below). A two-stage calculation was thus performed to evaluate results. First, 5% anhydrite was removed from the John_Klein composition to put SO₃ at similar concentrations in both samples, and broadly consistent with mapping veins in drill hole walls (4). Second, two gain-loss calculations were performed assuming Ti and Al, respectively, are constant between samples. Elements enriched (taken as ≥5% in both calculations) in Cumberland include Fe, Ca, Cl, Br, Ni and Ge. Elevated Ca is difficult to interpret given the Ca-sulfate in fractures but elevated Fe, Cl, Br and Ni are consistent with small amounts of a minor mineral such as akaganeite, identified by XRD, forming at least part of the concretion cement (4).

ChemCam and APXS analyses of isopachous cements within early diagenetic raised ridges indicate the presence of a Mg-Fe-Cl rich phase (or assemblage). ChemCam confirms that the amount of MgO is as high as ~18%, and in places is accompanied by elevated Li ([Fig. 5A](#)). The observation that Li and Mg are not well correlated across the different layers of isopachous cements (e.g., right hand side of [Fig. 5A](#) image) suggests a complex origin. APXS rasters on the raised ridge target McGrath further indicates elevated Fe and that both Mg and Fe correlate with Cl, although enrichment of any chloride phase or oxychlorine compound explains only a tiny part of the Mg-Fe variation ([Fig 5B](#)). A mass balance calculation using the highest and lowest APXS MgO analyses from the McGrath raster (McGrath-R1 and -R2) and assuming the phase is ~20% of the rock indicates a composition of SiO₂~45%; FeO_T~35%; MgO~18%, Cl~3% and ~1,300-1,500 ppm each for Ni, Zn and Br ([Supplemental Information - Mass Balance Calculations; Supplemental Table S7](#)). Such a composition cannot be accommodated by any single phase identified in the drilled samples by XRD, but perhaps is consistent with a mixture of Mg-rich, Al-deficient smectitic clay (e.g., hectorite, stevensite) and halogen-bearing Fe-oxides (e.g., akaganeite).

Late Diagenetic Features: Both ChemCam and APXS provide constraints on the mineralogy of cross-cutting late diagenetic light-toned fractures, including filled minibowls. ChemCam shots on these features ([Fig. 5C](#)) show elevated Ca, S and in places H, indicating multiple hydration states of Ca-sulfate. ChemCam also measured elevated Sr content (up to 450 ppm) in the fracture fills ([Fig. 5C](#)), as expected for Ca-sulfate (46). The presence of multiple Ca-sulfate minerals is also consistent with ChemMin XRD analyses that identified anhydrite and bassanite (but not gypsum) and MastCam VNIR spectroscopy that suggests that some fracture fills are hydrated, possibly indicating gypsum (4). Finally, APXS raster analysis on the fracture fill target Sayunei also

indicates the presence of Ca-sulfates through a correlation between CaO and SO₃, the slope of which is consistent with CaSO₄ stoichiometry (Fig. 5D).

The composition of the dike-like “snake” feature may bear on its origin and Fig. 6 shows comparison plots between the dike-like feature (Snake_River target) and average lower Sheepbed member (Fig. 6A), the Gillespie Lake member sample (Fig. 6C) and average Shaler member (Fig. 6C). The Snake_River major element composition is most similar to sedimentary rocks in the lower part of the Yellowknife Bay formation and best matches the lower Sheepbed member for major elements; it differs from the Gillespie Lake member for both major and trace elements. Although overlap exists with individual samples of the heterogeneous Shaler member, the “snake” does not compare favorably to the Shaler average for a number of elements suggesting it did not result from infall of overlying sediment into a fracture. We conclude from these comparisons that the composition of the snake is consistent with a sedimentary dike, as suggested by *Grotzinger et al.* (2) from stratigraphic relationships, intruded from the Sheepbed or unexposed sediments at lower stratigraphic levels and not currently exposed. In detail, its chemical composition differs from both the Sheepbed and Gillespie Lake (e.g., higher Cr) and thus suggests an origin from a different, presumably lower, stratigraphic level.

Discussion: Elemental geochemistry reveals a fundamental provenance change during deposition of the Yellowknife Bay formation. Clastic sediments of the Sheepbed and Gillespie Lake members were derived from a source similar to the average Martian crust but slightly more mafic and Fe-rich (SiO₂~ 46% vs 49%; FeO_T~21.5% vs 18%), whereas high-K alkaline igneous rocks dominate the Point Lake provenance and contribute to Shaler provenance. An explanation for the change in provenance may be related to erosional evolution of drainage basins feeding the alluvial fan system. Dncutting fluvial channels in the catchment of the fan system may have encountered a distinct alkaline basalt bedrock lithology (likely related to Jake_Matijevic-type composition) or captured a drainage underlain by such a lithology leading to the abrupt change in sediment provenance. On the other hand, alkaline basalts of the type suggested to be incorporated in Point Lake and Shaler sediments are rare on Earth (47) and having them represent a dominant provenance component in distal facies of a fluvial system is unexpected and could suggest that such rocks, which have also been observed in Gusev Crater (48), are more common on Mars than previously thought (48,49). An alternative possibility is that an exotic source of alkaline basalts was locally introduced into the basin, by way of volcanic ash or flows, and reflecting relatively small volumes of alkaline basalt that in turn were locally recycled and preserved as volcanoclastic layers. This scenario is consistent with the observation that high-K signatures appear restricted to certain beds within the Shaler member. Given the limited stratigraphic distribution that has been studied (Point Lake and Shaler members exhibiting the high-K signature represent only ~2 meters of a <5 meter section) it is not possible to distinguish whether local or more regionally exposed high-K lithologies caused the provenance change and thus the scale of any potential alkaline igneous province is not well constrained from the sedimentary data.

Martian soils likely contain a small (~1-3%) meteoritic component (50) and estimates of crustal composition (notably Ni) are derived by assuming a 2% meteoritic soil component (12). Sheepbed mudstones, if deposited in an ancient lake that

represented the terminus of a watershed, might be expected to contain meteoritic material that was swept into the basin. Certainly provenance effects alone can explain the levels of Ni (~450-850 ppm) in the Sheepbed member given the slightly more mafic and Fe-rich composition, compared to average Martian crust. On the other hand, trace element data are also consistent with a modest meteoritic contribution. [Figure 4B](#) models the effects of adding a CI composition to average Martian crust and to one of the brushed lower Sheepbed samples (Ekwir_Brush) and shows that the low Cr/Ni and Zn/Ni ratios of the Sheepbed member are consistent with ~1-4% CI component, with a larger amount in the upper part of the member. For typical CI-type chondritic compositions (51), a 1-4% meteoritic component would also deliver ~300-1,200 ppm organic C, consistent with low levels of carbon detected by SAM (4).

In the absence of a fossil record, sediment chemistry is one of the few tools available to evaluate paleoclimate, by constraining chemical weathering intensity (10,52,53). Low CIA values and positions on A-CN-K and A-CN-K-FM diagrams for the Yellowknife Bay formation ([Fig. 2](#)) indicate very limited chemical weathering prior to deposition. The similarity between major elements of the Gillespie Lake bedload-dominated sandstones and Sheepbed member suspended load-dominated mudstones also suggests that the fluvial system carried a very high ratio of solid to dissolved river loads (L_s/L_d), which in turn results from both arid conditions and rapid erosion and transport (53,54) and could have been further enhanced by cold conditions that would kinetically inhibit chemical weathering reactions. Accordingly, Yellowknife Bay formation geochemistry is consistent with some combination of a highly arid, possibly frigid, climate and/or a high relief fluvial system, and probably both. On early Mars, impact processes may have aided in the generation of sedimentary particles, increasing the efficiency of physical denudation (55). Surface waters with low L_d significantly contrasts with the high ionic strength ancient surface waters suggested at Meridiani Planum (56), even though both apparently record evidence of an arid climate system. In spite of the suggested arid conditions, relatively small amounts of chemical sedimentation (e.g., sulfates, carbonates, chlorides) may be expected in the Yellowknife Bay sedimentary system. In addition, to the degree that surface water contributes to the regional groundwater system, it would also tend to promote dilute, circum-neutral subsurface aqueous conditions.

Elemental geochemistry provides constraints on diagenetic history. The uniform bulk rock compositions of Sheepbed mudstones is particularly important, along with its suite of complex diagenetic features, which suggest post-depositional aqueous alteration took place at combined low water/rock ratios and pH levels modest enough that mineralogical changes took place under nearly isochemical conditions; very little mass has been removed from the system. Therefore, the broad array of secondary minerals identified by XRD, including saponitic phyllosilicates, magnetite, akaganeite, hematite(?) and perhaps a significant part of the amorphous component, needs to be explained by plausible reactions taking place within the sediment (4). One important exception is that textural and geochemical relationships indicate Ca-sulfates, found in fractures, voids and minibowls, were later “added” to the rock and not formed by local redistribution of elements during the earlier stage of diagenesis that transformed the Sheepbed sediment to rock. Accordingly, at least two distinct diagenetic fluid events took place with distinct fluid chemistry. The first resulted in the mineral assemblage within the host sediment

(and perhaps the Fe-Mg-Cl-rich assemblage associated with early diagenetic raised ridges). Plausible reactions that could be involved include olivine (+Al) \Rightarrow saponite + magnetite (4) and pyrrhotite (+pyrite?) \Rightarrow akaganeite (\Rightarrow hematite?), the latter of which would be promoted by Cl⁻-bearing fluids that also in turn could have promoted concretion formation. Sometime after lithification, a second fluid event, presumably originating from deeper within the section and associated with fracturing of the mudstone, injected fluids that became saturated with respect to Ca-sulfate (typically early precipitated minerals in evolving brines) due to changing chemistry and/or pressure-temperature conditions. These fluids precipitated sulfates within the fractures, and filled any void spaces that the fractures intersected, including the minibowls. Although considerable modeling and experimental effort will be required to fully understand these processes, it is possible to construct simple forward thermochemical aqueous models broadly consistent with these observations ([Supplemental Information – Thermochemical Modeling](#)).

Our findings add to the growing evidence for highly diverse sedimentary environments on early Mars (57,58). The Burns formation of Meridiani Planum is the only sedimentary sequence that has been studied in situ in comparable detail and is of similar age - if anything even older (20,55,58,59). Although both represent clastic sedimentation derived from basalt sources and influenced by complex groundwater diagenesis, the sedimentary history is strikingly different. For example, where the Burns formation preserves evidence for very low pH and very high ionic strength groundwater, the Yellowknife Bay formation had relatively dilute circum-neutral groundwater. Where the Burns formation is dominated by chemical constituents (sulfates, chlorides) derived from evaporation of acidic brines, Yellowknife Bay mudstones contain very little in the way of chemical constituents and the secondary mineralogy formed mostly within a largely closed geochemical system. Where the basaltic debris within the Burns was substantially weathered, Yellowknife Bay detritus appears to be essentially unweathered. Orbital spectroscopic mapping suggests that surface environmental conditions on early Mars evolved from circum-neutral clay-rich to acidic sulfate-rich settings (60) but it would appear, just like on Earth where evolving global environments are also reflected in the broad sweep of the sedimentary record (61), that when faced with rocks on the ground, geological complexity is apparently inevitable. The upcoming exploration by *Curiosity*, of the thick sedimentary sequence constituting Mount Sharp (Aeolis Mons) in the center of Gale crater, thus provides the next opportunity to better understand the evolution of the early Martian surface.

References and Notes:

1. Names have been assigned to certain areographic features by the Mars Science Laboratory (MSL) team for planning and operations purposes. The names are not formally recognized by the International Astronomical Union.
2. J. P. Grotzinger et al., A habitable fluvio-lacustrine environment at Yellowknife Bay, Gale crater, Mars. *Science*, this issue (2013).
3. D. W. Ming et al., Organic, volatile, and isotopic compositions of a sedimentary rock in Yellowknife Bay, Gale crater, Mars. *Science*, this issue (2013).

4. D. T. Vaniman et al., Mineralogy of a mudstone on Mars. *Science*, this issue (2013).
5. H. W. Nesbitt, G. M. Young, Early Proterozoic climates and plate motions inferred from major element chemistry of lutites. *Nature* 299, 715-717 (1982).
6. H. W. Nesbitt, G. M. Young, Petrogenesis of sediments in the absence of chemical weathering: Effects of abrasion and sorting on bulk composition and mineralogy. *Sedimentology* 43, 341-358 (1996).
7. S. M. McLennan, S. Hemming, D. K. McDaniel, G. N. Hanson, Geochemical approaches to sedimentation, provenance, and tectonics, in *Processes Controlling the Composition of Clastic Sediments*, M. J. Johnsson, A. Basu, Eds. *Geol. Soc. Amer. Spec. Paper* 284, 21-40 (1993).
8. H. W. Nesbitt, G. M. Young, S. M. McLennan, R. R. Keays, Effects of chemical weathering and sorting on the petrogenesis of siliciclastic sediments, with implications for provenance studies. *J. Geol.* 104, 525-542 (1996).
9. C. M. Fedo, G. M. Young, H. W. Nesbitt, J. M. Hanchar, Potassic and sodic metasomatism in the Southern Provenance of the Canadian Shield: Evidence from the Paleoproterozoic Serpent Formation, Huronian Supergroup, Canada. *Precambrian Res.* 84, 17-36 (1997).
10. H. W. Nesbitt, Petrogenesis of siliciclastic sediments and sedimentary rocks, in *Geochemistry of Sediments and Sedimentary Rocks*, D. R. Lentz, Ed. *Geol. Assoc. Canada GeoText* 4, 39-51 (2003).
11. S. R. Taylor, S. M. McLennan, *The Continental Crust: Its Composition and Evolution* (Blackwells, Oxford, 1985).
12. S. R. Taylor, S. M. McLennan, *Planetary Crusts: Their Composition, Origin and Evolution* (Cambridge Univ. Press, Cambridge, 2009).
13. G. M. Young, H. W. Nesbitt, Paleoclimatology and provenance of the glaciogenic Gowganda Formation (Paleoproterozoic), Ontario, Canada: A chemostratigraphic approach. *Geol. Soc. Amer. Bull.* 111, 264-274 (1999).
14. P. Michalopoulos, R. C. Aller, Rapid clay mineral formation in Amazon Delta sediments – reverse weathering and oceanic elemental cycles. *Science*, 270, 614-617 (1995).
15. M. A. Chan et al., Models of iron oxide concretion formation: Field, numerical, and laboratory comparisons. *Geofluids*, 7, 356-368 (2007).
16. B. C. Clark, et al., Chemistry and mineralogy of outcrops at Meridiani Planum. *Earth Planet. Sci. Lett.* 240, 73-94 (2005).
17. S. M. McLennan et al., Provenance and diagenesis of the evaporite-bearing Burns formation, Meridiani Planum, Mars. *Earth Planet. Sci. Lett.* 240, 95-121(2005).
18. J. A. Hurowitz et al., Mixing relationships and the effects of secondary alteration in the Wishstone and Watchtower classes of Husband Hill, Gusev Crater, Mars. *J. Geophys. Res.-Planets*, 111, E12S14, doi:10.1029/2006JE002795 (2006).

19. A. H. Knoll et al., Veneers, rinds, and fracture fills: Relatively late alteration of sedimentary rocks at Meridiani Planum, Mars. *J. Geophys. Res.-Planets*, 113, E06S16, doi:10.1029/2007JE002949 (2008).
20. S. M. McLennan and J. P. Grotzinger, The sedimentary rock cycle of Mars, in *The Mars Surface: Composition, Mineralogy and Physical Properties*, J. F. Bell III, Ed., pp. 541-577, Cambridge Univ. Press (Cambridge, 2008).
21. S. W. Squyres et al., Ancient impact and aqueous processes at Endeavour crater, Mars. *Science*, 336, 570-576 (2012).
22. B. Ehlmann et al., Subsurface water and clay mineral formation during the early history of Mars. *Nature*, 114, 53-60 (2011).
23. R. Gellert et al. Initial MSL APXS activities and observations at Gale crater, Mars. *44th Lunar Planet. Sci. Conf.*, Abst. #1432, The Woodlands, 18-22 March (2013).
24. S. Maurice et al., The ChemCam instrument suite on the Mars Science Laboratory (MSL) rover: Science objectives and mast unit description. *Space Sci. Rev.*, 170, 95-106 (2012).
25. R. C. Wiens et al., The ChemCam instrument suite on the Mars Science Laboratory (MSL) rover: Body unit and combined system tests. *Space Sci. Rev.*, 170, 167-227 (2012).
26. A. S. Yen et al., An integrated view of the chemistry and mineralogy of Martian soils. *Nature*, 436, 49-54 (2004).
27. D. F. Blake et al., Curiosity at Gale: Characterization and analysis of the Rocknest sand shadow. *Science* (in press) (2013).
28. H. W. Nesbitt, R. E. Wilson, Recent chemical weathering of basalts. *Am. J. Sci.*, 292, 740-777 (1993).
29. In order to focus on relationships among silicate and oxide mineralogy A-CN-K and A-CN-K-FM diagrams normally correct CaO for the presence of carbonates and sedimentary Ca-phosphates (CaO*) and in rare cases correct Na₂O for the presence of halite (Na₂O*). In Martian settings attempts at making corrections for chemical constituents have proven non-unique because mineralogical determinations are either incomplete or do not exist and non-silicate and non-oxide mineralogy is both uncertain and complex, involving a variety of Ca-, Mg- and Fe-sulfates, chlorides, perchlorates and in some cases carbonates. Accordingly, bulk analyses are used in formulating these diagrams and the CIA values and the possibility of non-silicate and non-oxide phases must be considered when making interpretations.
30. M. E. Schmidt et al., Geochemical diversity in first rocks examined by the Curiosity rover in Gale crater: Evidence and significance of an alkali and volatile-rich igneous source. *J. Geophys. Res.-Planets* (submitted, 2013).
31. K. Stamateloupoulou-Seymour, D. M. Francis, An Archean ultramafic turbidite from Lac Guyer, James Bay area, Quebec, Canada. *Can. J. Earth Sci.*, 17, 1576-1582 (1980).

32. H. W. Nesbitt et al., Major and trace element geochemistry and genesis of supracrustal rocks of the North Spirit Lake greenstone belt, NW Ontario, Canada. *Precambrian Res.*, 174, 16-34 (2009).
33. S. Saha et al., The influence of flood basaltic source terrains on the efficiency of tectonic discrimination diagrams: An example from the Gulf of Khambhat, western India. *Sediment. Geol.*, 228, 1-13 (2010).
34. L. L. Griffith, E. L. Shock, Hydrothermal hydration of Martian crust: Illustration via geochemical model calculations. *J. Geophys. Res.-Planets*, 102, 9135-9143 (1997).
35. J. A. Hurowitz et al., Experimental epithermal alteration of synthetic Los Angeles meteorite: Implications for the origin of Martian soils and identification of hydrothermal sites on Mars. *J. Geophys. Res.-Planets*, 110, E07002, doi:10.1029/2004JE002391 (2005).
36. M. V. Naumov, Principal features of impact-generated hydrothermal circulation systems: Mineralogical and geochemical evidence. *Geofluids*, 5, 165-184 (2005).
37. N. J. Tosca et al., Geochemical modeling of evaporation processes on Mars: Insight from the sedimentary record at Meridiani Planum. *Earth Planet. Sci. Lett.*, 240, 122-148 (2005).
38. J. A. Hurowitz et al., In-situ and experimental evidence for acidic weathering on Mars. *J. Geophys. Res.* 111, E02S19, doi:10.1029/2005JE002515 (2006).
39. P. L. King and H. Y. McSween Jr., Effects of H₂O, pH and oxidation state on the stability of Fe-minerals on Mars. *J. Geophys. Res.-Planets*, 110, E12S10, doi:10.1029/2005JE002482 (2005).
40. H. Blatt, G. Middleton, R. Murray, *Origin of Sedimentary Rocks* (Prentice-Hall, Englewood Cliffs, 1972).
41. G. M. Young, H. W. Nesbitt, Processes controlling the distribution of Ti and Al in weathering profiles, siliciclastic sediments and sedimentary rocks, *J. Sed. Res.*, 68, 448-455 (1998).
42. N. C. Martinez et al., Local and regional geochemical signatures of surface sediments from the Cariaco Basin and Orinoco Delta, Venezuela, *Geology*, 38, 159-162 (2010).
43. Basaltic Volcanism Study Project, *Basaltic Volcanism on the Terrestrial Planets* (Pergamon Press, New York, 1981).
44. R. Slingerland, N.D. Smith, Occurrence and formation of waterlaid placers. *Ann. Rev. Earth Planet. Sci.*, 14, 113-147 (1986).
45. L.-H. Chan et al., Lithium and lithium isotope profiles through the upper oceanic crust: A study of seawater-basalt exchange at ODP Sites 504A and 896A. *Earth Planet. Sci. Lett.*, 201, 187-201 (2002).
46. F. H. Lu, W. J. Meyers, G. N. Hanson, Trace elements and environmental significance of Messinian gypsum deposits, the Nijar Basin, southeastern Spain. *Chem. Geol.*, 192, 149-161 (2002).

47. E. M. Stolper et al. The petrochemistry of Jake_M: A Martian mugearite. *Science* (in press, 2013)
48. H. Y. McSween et al., Alkaline volcanic rocks from the Columbia Hills, Gusev Crater, Mars. *J. Geophys. Res.-Planets*, 111, E09S91, doi:10.1029/2006JE002698 (2006).
49. H. Nekvasil et al., Linking the Chassigny meteorite and the Martian surface rock Backstay: Insights into igneous crustal differentiation processes on Mars. *Meteor. Planet. Sci.*, 44, 853-869 (2009)
50. A. S. Yen et al., Nickel on Mars: Constraints on meteoritic material at the surface. *J. Geophys. Res.-Planets*, 111, E12S11, doi:10.1029/2006JE002797 (2006).
51. R. Hutchison, *Meteorites: A Petrologic, Chemical and Isotopic Synthesis* (Cambridge Univ. Press, Cambridge, 2004).
52. L. J. Suttner, P. K. Dutta, Alluvial sandstone composition and paleoclimate, I. Framework mineralogy. *J. Sed. Pet.*, 56, 329-345 (1986).
53. A. D. Stewart, The ratio of mechanical to chemical denudation in alluvial systems, derived from geochemical mass balance. *Trans. Roy. Soc. Edinburgh: Earth Sci.*, 84, 73-78 (1993).
54. J.-M. Martin, M. Meybeck, Elemental mass-balance of material carried by major world rivers. *Marine Chem.*, 7, 173-206 (1979).
55. J. P. Grotzinger, A. G. Hayes, M. P. Lamb, S. M. McLennan, Sedimentary processes on Earth, Mars, Titan, and Venus, in *Comparative Climatology of Terrestrial Planets*, S. J. Mackwell et al., Eds., pp. xxx-xxx (Univ. Arizona Press, Tucson, in press 2013).
56. N. J. Tosca et al., Physicochemical properties of concentrated Martian surface waters. *J. Geophys. Res.-Planets*, 116, E05004, doi:10.1029/2010JR003700 (2011).
57. S. L. Murchie et al., A synthesis of Martian aqueous mineralogy after 1 Mars year of observations from the Mars Reconnaissance Orbiter. *J. Geophys. Res. - Planets*, 114, 1-30 (2009).
58. J. P. Grotzinger, R. E. Milliken, Eds., *Sedimentary Geology of Mars. SEPM Spec. Publ. 12* (Society for Sedimentary Geology, Tulsa, 2012).
59. S. W. Squyres, A. H. Knoll, Eds., *Sedimentary Geology at Meridiani Planum, Mars* (Elsevier, Amsterdam, 2005)
60. J.-P. Bibring et al., Global mineralogical and aqueous Mars history derived from OMEGA/Mars Express data. *Science*, 312, 400-404 (2006).
61. R. M. Hazen et al., Mineral evolution. *Amer. Mineral.*, 93, 1693-1720 (2008).
62. J. L. Campbell et al., Calibration of the Mars Science Laboratory Alpha Particle X-ray spectrometer. *Space Sci. Rev.*, 170, 319-340 (2012).
63. L. M. Thompson et al., BT-2 calibration target for the Mars Science Laboratory Alpha Particle X-ray spectrometer: Characterization and alkali basalt Martian

- analogue. 44th *Lunar Planet. Sci. Conf.*, Abst. #2190, The Woodlands, 18-22 March (2013).
64. R. Gellert et al., Alpha Particle X-ray spectrometer (APXS): Results from Gusev Crater and calibration report. *J. Geophys. Res.-Planets*, 111, E02S05, doi:10.1029/2005JE002555.
 65. R. C. Wiens R.C. et al., Pre-flight calibration and initial data processing for the ChemCam laser-induced breakdown spectroscopy instrument on the Mars Science Laboratory rover. *Spectrochim. Acta*, B82, 1-27 (2013).
 66. S. M. Clegg et al., Quantitative remote laser induced breakdown spectroscopy by multivariate analysis. *Spectrochim. Acta*, B64, 79-88 (2009).
 67. M. H. Reed et al., *Users Guide for CHIM-XPT* (University of Oregon, 2010).

Acknowledgments: Much of this research was carried out at the Jet Propulsion Laboratory, California Institute of Technology, under contract with NASA. Development and operation of the ChemCam and APXS instruments were also supported by funds from the French Space Agency, CNES and the Canadian Space Agency. Organizations supporting research include NASA, the Canadian Space Agency and NSERC (Canada). We are grateful to the MSL engineering and management teams for making the mission and this scientific investigation possible and to science team members who contributed to mission operations. The senior author (SMM) thanks Lamont-Doherty Earth Observatory of Columbia University, and especially Sidney Hemming, for hospitality during a sabbatical when the manuscript was being prepared.

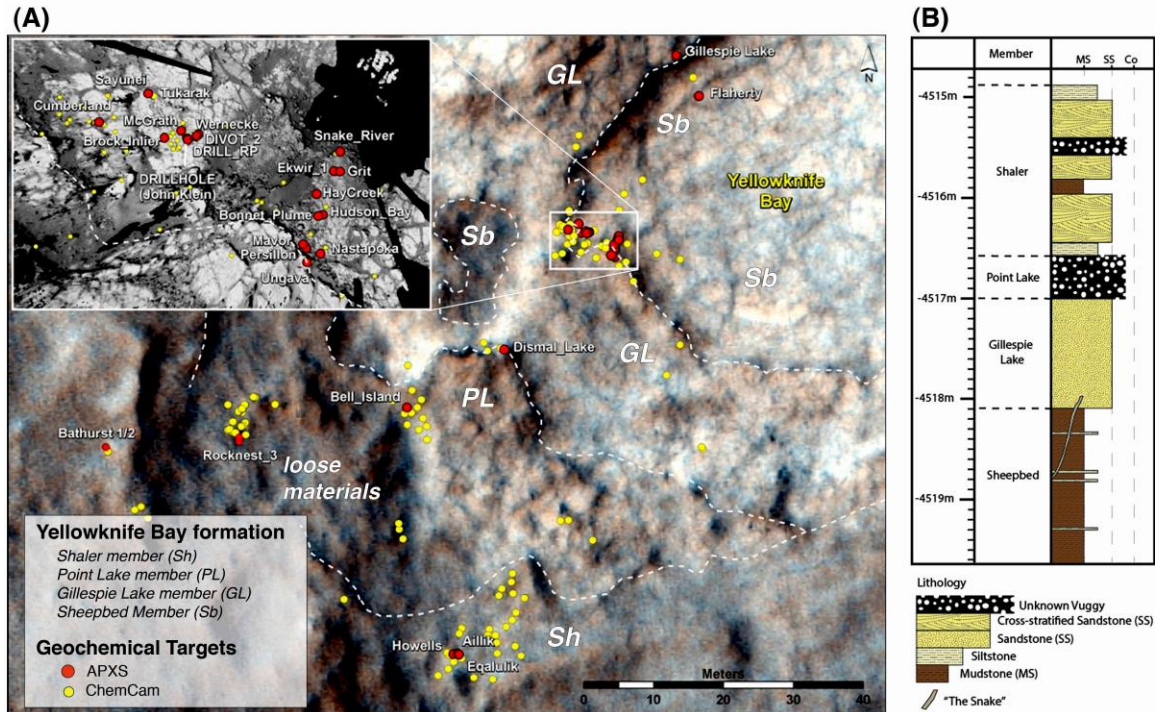


Fig. 1. (A) HiRISE image (part of PSP_010573_1755) showing geological relationships of the Yellowknife Bay formation and location and names of APXS analyses and locations of ChemCam LIBS analyses and names of ChemCam targets, Tukarak and McGrath (also an APXS target), discussed in the text. Inset shows expanded Navigational camera overhead projection of the region where drilling of the Sheepbed member took place (John_Klein and Cumberland) and where the Selwyn Section (targets between Snake_River and Ungava) was examined. (B) Stratigraphic section of the Yellowknife Bay formation at Yellowknife Bay. Also shown is the stratigraphic relationship of the cross-cutting dike-like feature termed “the snake” (adapted from ref. 2).

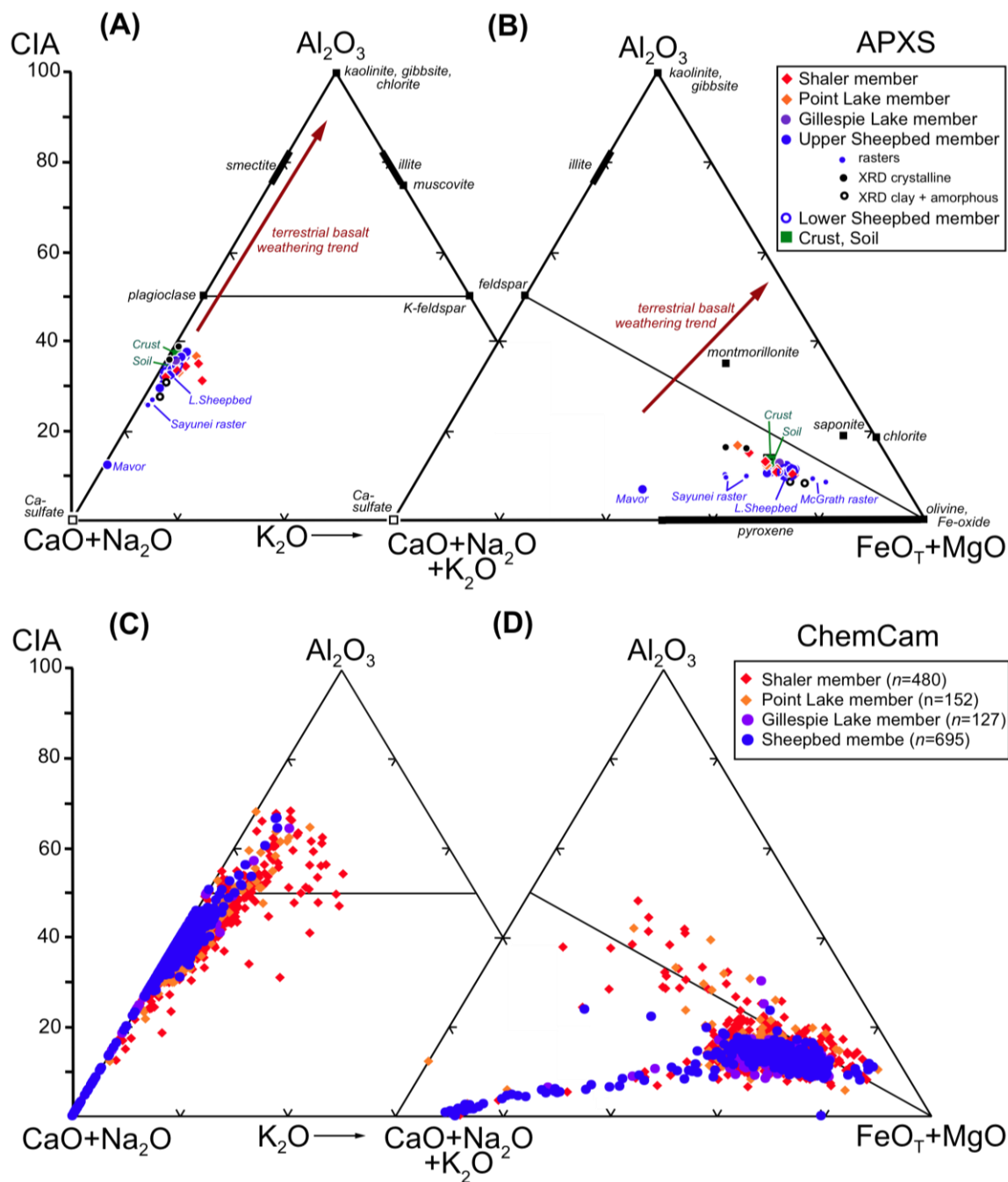


Fig. 2. A-CN-K and A-CN-K-FM diagrams (A,B) for APXS data; (C,D) for ChemCam data. Shown for reference are the CIA scale (measured on (A) and (C) only), average Martian crust (12) and local soil (27), modeled compositions of John_Klein and Cumberland crystalline and clay+amorphous materials (4), and arrows representing typical trends observed for terrestrial weathering profiles on basalts (28). The greater scatter for ChemCam data results mainly from its higher spatial resolution and thus records analyses of individual phases (e.g., feldspar, Ca-sulfate) and mixtures of small numbers of phases.

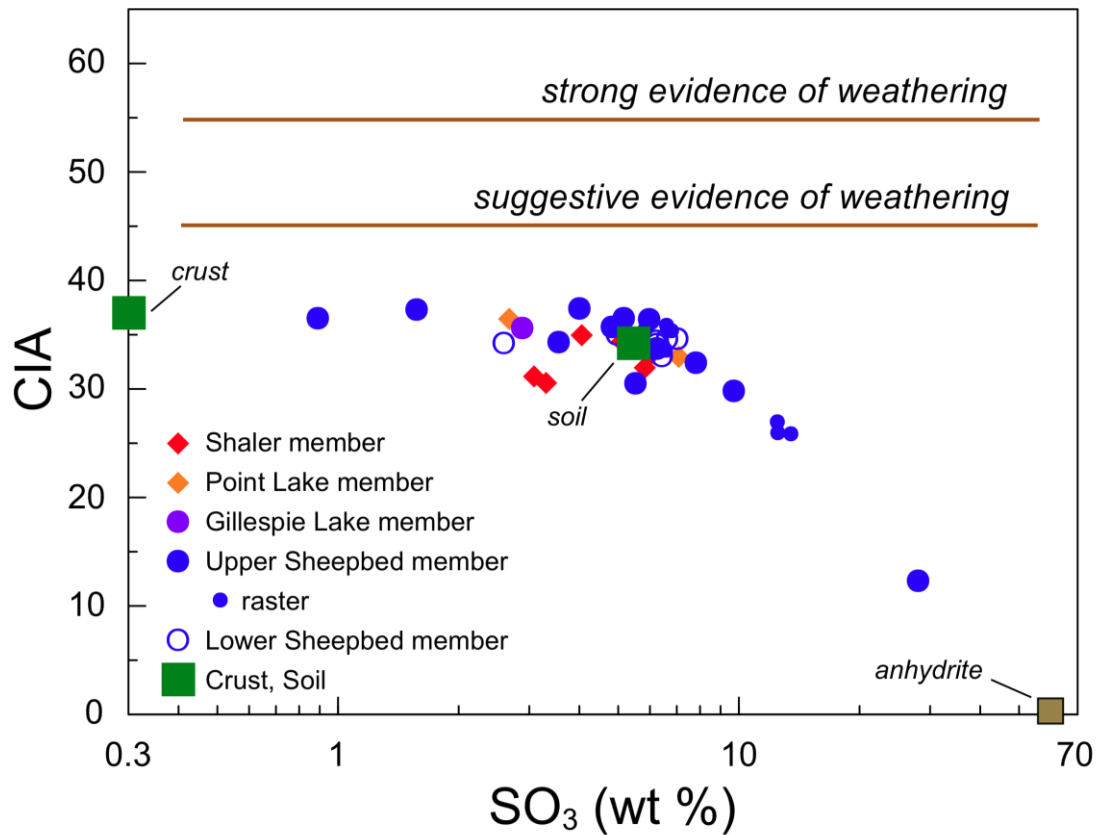


Fig. 3. Plot of CIA versus SO₃ contents for Yellowknife Bay formation APXS analyses. Also shown for reference is the composition of anhydrite (CaSO₄). Note that at high SO₃ the CIA value falls, indicating the presence of Ca-sulfates, but at low SO₃, the CIA value levels off to typical igneous values consistent with none of these samples having seen a significant weathering history.

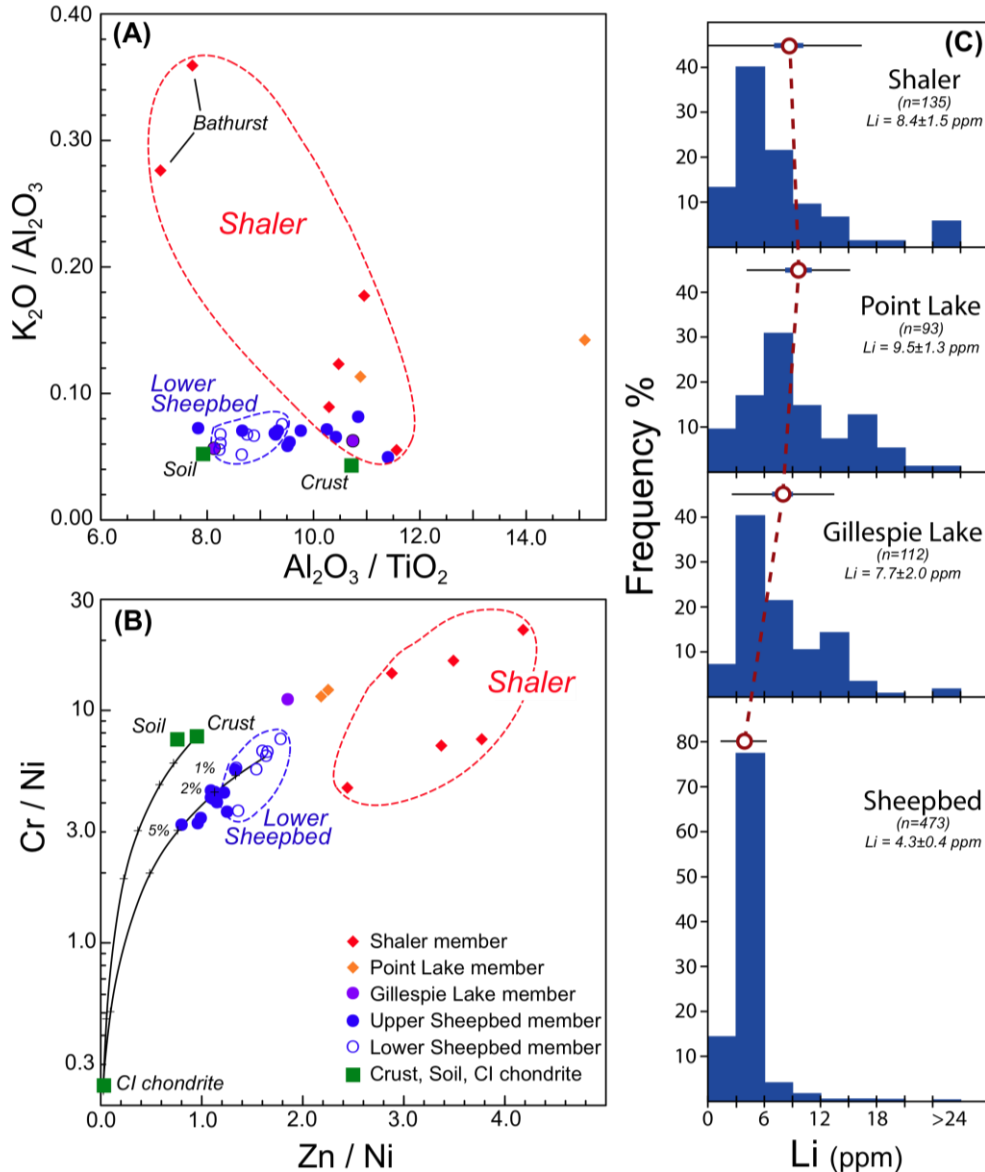


Fig. 4. Plots of Yellowknife Bay formation (A) APXS K_2O/Al_2O_3 versus Al_2O_3/TiO_2 , (B) APXS Cr/Ni versus Zn/Ni ; (C) histograms of ChemCam Li abundances also showing mean (red circle), standard deviation (black bar) and 95% confidence interval (blue bar), highlighting stratigraphic variations. The Sheepbed member has relatively uniform and low K_2O/Al_2O_3 , Al_2O_3/TiO_2 , Cr/Ni , Zn/Ni ratios and Li abundances. The overlying members differ from the Sheepbed to varying degrees with the Point Lake and Shaler members being variably enriched in K_2O/Al_2O_3 , consistent with introduction of alkaline-rich basaltic provenance components higher in the section. The Sheepbed member also shows slight differences in Al_2O_3/TiO_2 , between upper and lower parts, consistent with slightly differing mafic provenance. Shown on Fig. 2B are mixing lines between average Martian crust and the Ekwir_Brush target and average CI chondrite. Zn/Ni and Cr/Ni are consistent with either a more Ni-rich provenance in the upper Sheepbed and/or small meteoritic components (~1-4%). The Sheepbed member is characterized by low and uniform Li abundances whereas overlying units have higher and more variable Li.

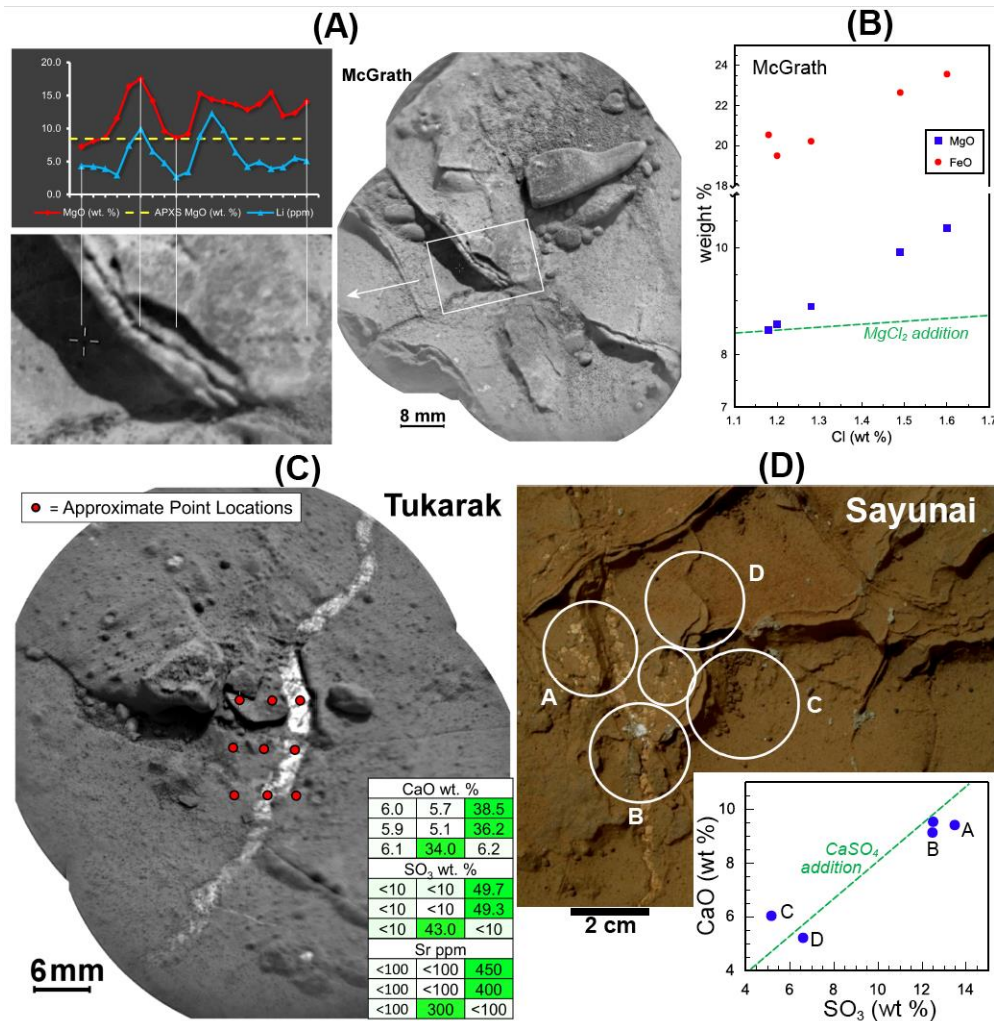


Fig. 5. Geochemical constraints on diagenetic features within the Yellowknife Bay formation. (A) ChemCam RMI image of the McGrath target “raised ridge” that is dipping gently to the upper right. Inset shows LIBS MgO and Li transects for 20 shots taken across the feature. Shown for reference is the average MgO of McGrath, determined by APXS. Note elevated and correlated Mg and Li at the site of the raised ridge. Also note that elevated Mg (but not Li) is observed on the right hand side that likely represents the outer layer of the cement, exposed on the dipping surface. (B) APXS raster analysis for McGrath showing elevated Fe and Mg that correlate with Cl. A model of $MgCl_2$ addition is shown to illustrate that the correlation is not due simply to the presence of chloride phases. (C) ChemCam RMI image of a late diagenetic light-toned fracture at the Tukarak target. Location of a 3x3 LIBS raster is shown and results for Ca, S and Sr, relative to their position in the raster, are given in the inset table. Elevated Ca, S and Sr characterize all shots on light-toned material, consistent with Ca-sulfate. In some analyses of these features, elevated H is also observed suggesting variable Ca-sulfate hydration states. (D) APXS raster analysis on late diagenetic light-toned fracture at the Sayunai target. Inset shows plot of CaO versus SO_3 with a model illustrating the effects of $CaSO_4$ addition are consistent with the correlation.

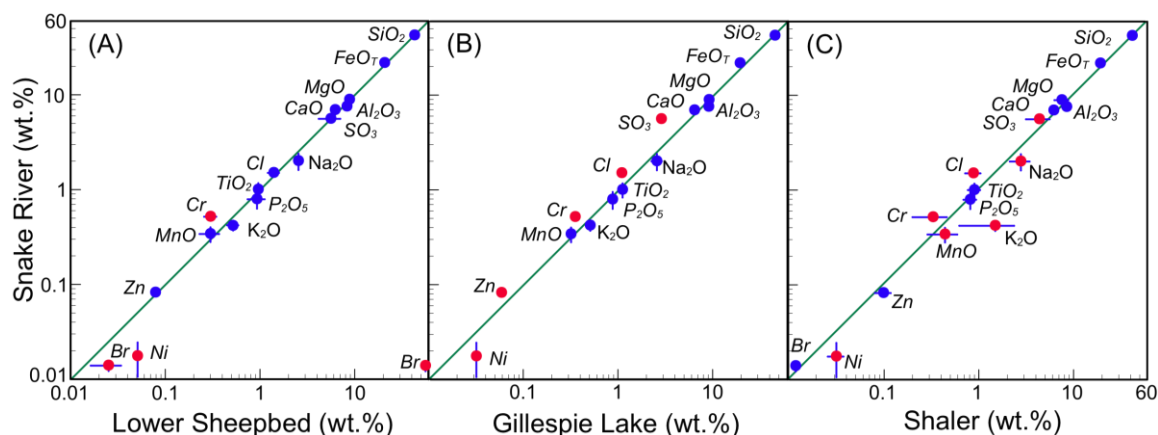


Fig. 6. Comparison diagrams for the dike-like feature (Snake_River target) versus (A) lower Sheepbed member average, (B) Gillespie Lake member sample and (C) Shaler member average. The diagonal green line represents equal compositions. Error bars (if larger than the symbol size) represent two sigma errors for individual samples (Snake_River, Gillespie Lake) and one standard deviation on the mean for averages (Lower Sheepbed member, Shaler member). Significant differences in composition are shown as red symbols. The Snake_River sample is closest in composition to the average lower Sheepbed member but with lesser abundances of Ni and Br and a higher abundance of Cr.

Supplementary Materials:

Figure S1

APXS Methods

Tables S1-S7

ChemCam Methods

Mass Balance Calculations

Thermochemical Modeling of Diagenesis at Yellowknife Bay

Figure S2

References (62-67)

Supplementary Materials:

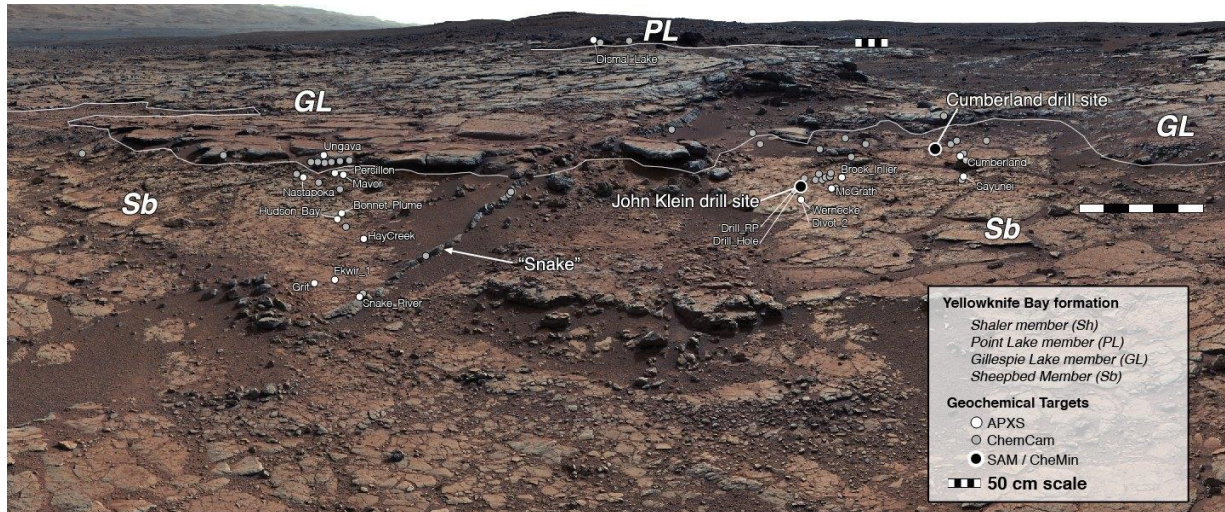


Fig. S1. Mastcam mosaic of Yellowknife Bay formation with locations of visible APXS (white dots; including target names) and ChemCam targets (grey dots) from Fig. 1. Also shown are APXS targets where drilling and SAM and CheMin (XRD) measurements were made (black dots) and approximate locations of contacts between the Sheepbed, Gillespie Lake and Point Lake members. View from base of exposed section through the Sheepbed, Gillespie Lake and Point Lake members. Both scale bars are 50 centimeters long with 10 centimeter spaces section; the lower scale is about 8 meters from the Curiosity rover position and the upper scale bar is about 30 meters away. The mosaic was acquired on sol 137 by the Mastcam-34 camera, sequence 818 (modified from Fig. 3 in ref. 2).

APXS Methods: The MSL APXS uses radioactive ^{244}Cm sources that excite geologic samples via PIXE (“particle-induced X-ray emission”) and XRF (X-ray fluorescence). Characteristic X-rays are emitted from the sample as a result of these two processes and are detected by the APXS instrument. The characteristic X-ray energies are unique for each element and their intensities are used to determine the weight fraction abundances of major, minor, and some trace (Cr, Ni, Zn, Br, Ge) elements (23,62). Penetration depths to the region above which 90% of the observed X-rays originate increase as a function of Z and range from 2 to 80 μm for Na to Fe. A calibration standard (63) was sent to Mars with the rover to verify that the APXS calibration produced on Earth remains valid on Mars. A Peltier cooler permits the recording of

daytime spectra with integrations as short as 10 minutes. An aluminum contact sensor allows for reproducible instrument placement heights, which is valuable for determining accurate elemental abundances. In some instances, the position relative to the rover or the nature of the targeted geological material required stand-off distances of 1-3 cm in response to complexity of arm movement, or to prevent contamination of the APXS sources by fine-grained materials (i.e., tailings pile).

The APXS data reported here (Tables S1-S4) were reduced using an empirical peak-fitting and calibration routine that was developed for the Mars Exploration Rover (MER) APXS analyses (64). Varying stand-off distances are taken into account by a geometric normalization such that the total oxide content is normalized to 100 wt %. Statistical (2σ) errors were generated by the respective spectrum-fitting routines; these errors are functions of the overall spectral intensity and thus reflect duration and stand-off, and they are also increased by increasing temperature which causes greater peak overlap. These are summarized for the reported samples in Table S5. Statistical errors are significantly smaller than the uncertainties associated with the calibration, where the lighter elements especially show larger spreads that reflect the influence of the rock mineralogy on the matrix effects (62). One sample analyzed from the Gillespie Lake member (Ungava) has very large analytical 2σ errors (up to $>\pm 50\%$ relative for some elements including Na, P and Ni) due to short integration times and high temperatures and is not reported or discussed here.

Of the bedrock targets examined by the APXS in Yellowknife Bay, only two (Ekwir and Wernecke) were brushed by the Dust Removal Tool (DRT). Thus all other rock targets are variably covered with fine-grained dust and soil, and reported rock compositions contain contributions from both dust and the underlying rock. Dust contamination most affects S and Cl concentrations because these elements are enriched in Martian dust ($SO_3/Cl \sim 9$; 12,64). In addition, the X ray for the lightest elements detected by the APXS (Na, Mg, and Al) are largely contributed by the outer 2-3 μm of the target and thus surface dust coatings $>4 \mu m$ can block and/or contribute X-rays that combine with those from the underlying rock (30). As such, brushing of the Wernecke target resulted in a significant decrease in SO_3 (5.6 to 0.9 wt%) and a slight increase in Na_2O (2.7 to 3.0 wt%).

Table S1. APXS analyses of the lower part of the Sheepbed member listed in approximate stratigraphic order from the base.

	Flaherty	Costello	Grit	Ekwir_1	Ekwir_1 Brush	Hay_ Creek	Hudson Bay
SiO ₂	41.3	42.1	42.5	42.5	45.3	42.5	44.5
TiO ₂	0.95	1.03	1.01	0.95	0.88	0.92	1.01
Al ₂ O ₃	8.22	8.48	8.33	8.31	8.28	8.17	8.33
FeO _T	21.6	20.9	20.6	20.6	20.3	20.7	20.5
Cr ₂ O ₃	0.49	0.48	0.49	0.42	0.45	0.30	0.46
MnO	0.36	0.41	0.30	0.24	0.21	0.30	0.29
MgO	8.68	8.82	8.70	8.60	9.66	8.72	8.61
CaO	6.62	6.55	6.38	6.32	5.90	5.79	6.05
Na ₂ O	2.60	2.34	2.46	2.62	2.78	2.67	2.39
K ₂ O	0.42	0.47	0.50	0.56	0.62	0.54	0.56
P ₂ O ₅	0.93	0.60	1.04	1.05	1.08	1.07	0.73
SO ₃	6.42	6.22	6.23	6.23	2.59	6.62	4.96
Cl	1.18	1.36	1.25	1.42	1.78	1.43	1.41
CIA	32.9	34.3	34.0	33.6	34.1	34.5	34.9
CaO/Al ₂ O ₃	0.81	0.77	0.77	0.76	0.71	0.71	0.73
SiO ₂ /Al ₂ O ₃	5.03	4.97	5.10	5.11	5.47	5.21	5.34
Al ₂ O ₃ /TiO ₂	8.65	8.23	8.25	8.75	9.41	8.88	8.25
FeO _T /MgO	2.49	2.37	2.37	2.39	2.10	2.38	2.38
FeO _T /MnO	60.0	50.9	67.8	85.7	96.6	69.0	70.8
K ₂ O/Al ₂ O ₃	0.051	0.055	0.060	0.067	0.075	0.066	0.067
K ₂ O/Na ₂ O	0.16	0.20	0.20	0.21	0.22	0.20	0.23
Cr	3335	3253	3341	2855	3051	2086	3149
Ni	446	494	503	515	482	569	561
Zn	794	815	803	793	789	772	754
Ge	76	67	81	85	85	88	59
Br	323	165	308	315	327	107	218
Cr/Ni	7.48	6.59	6.64	5.54	6.33	3.67	5.61
Cr/Zn	4.20	3.99	4.16	3.60	3.87	4.27	4.18
Zn/Ni	1.78	1.65	1.60	1.54	1.64	1.36	1.34
S/Cl	2.18	1.83	2.00	1.76	0.58	1.85	1.41
Cl/Br	36.5	82.4	40.6	45.1	54.4	133.6	64.7
Selwyn Section	No	No	Yes	Yes	Yes	Yes	Yes
Analysis	As is	As is	As is	As is	Brush	As is	As is
Sol	129	129	150	149	150	162	161

Notes: Major elements in weight %; trace elements in ppm.

Abbreviations: FeO_T – total iron as FeO; CIA = 100*[Al₂O₃/(Al₂O₃+CaO+Na₂O+K₂O)] in mole fractions. No correction was made for chemical constituents (sulfates, carbonates, phosphates) and so CIA are minimum values.

Table S2. APXS analyses of the upper part of the Sheepbed member listed in approximate stratigraphic order from the base.

	Bonnet Plume	Sayunei_C	Divot2	Werneke Brush	McGrath R3	DrillHole_R4	Drill_RP
SiO ₂	44.6	43.9	43.6	46.9	43.2	42.1	41.4
TiO ₂	0.81	0.87	0.94	0.91	0.90	0.99	1.05
Al ₂ O ₃	8.44	9.43	8.71	8.88	8.56	8.57	8.22
FeO _T	20.0	18.6	20.6	20.5	19.5	20.1	20.3
Cr ₂ O ₃	0.43	0.47	0.42	0.41	0.43	0.40	0.35
MnO	0.24	0.35	0.29	0.28	0.28	0.29	0.30
MgO	8.90	8.81	9.89	9.80	8.56	9.03	8.33
CaO	5.83	6.01	6.16	5.40	6.63	7.73	6.89
Na ₂ O	2.47	2.89	2.98	3.04	2.61	3.00	2.48
K ₂ O	0.55	0.76	0.59	0.62	0.50	0.60	0.59
P ₂ O ₅	0.95	1.02	0.96	1.02	0.90	0.90	0.84
SO ₃	4.82	5.16	3.55	0.89	6.24	5.52	7.81
Cl	1.71	1.32	0.91	1.13	1.20	0.56	1.35
CIA	35.6	36.4	34.2	36.4	33.6	30.4	32.3
CaO/Al ₂ O ₃	0.69	0.64	0.71	0.61	0.77	0.90	0.84
SiO ₂ /Al ₂ O ₃	5.28	4.66	5.01	5.28	5.04	4.91	5.03
Al ₂ O ₃ /TiO ₂	10.42	10.84	9.27	9.76	9.51	8.66	7.83
FeO _T /MgO	2.25	2.11	2.08	2.09	2.28	2.23	2.43
FeO _T /MnO	83.5	53.2	71.1	73.2	69.6	69.3	67.5
K ₂ O/Al ₂ O ₃	0.065	0.081	0.068	0.070	0.058	0.070	0.072
K ₂ O/Na ₂ O	0.22	0.26	0.20	0.20	0.19	0.20	0.24
Cr	2910	3203	2842	2835	2972	2730	2363
Ni	896	580	711	694	710	621	649
Zn	862	770	819	794	777	755	814
Ge	42	47	90	99	55	69	79
Br	211	172	390	401	399	167	544
Cr/Ni	3.25	5.52	4.00	4.09	4.19	4.40	3.64
Cr/Zn	3.38	4.16	3.47	3.57	3.83	3.62	2.90
Zn/Ni	0.96	1.33	1.15	1.14	1.09	1.22	1.25
S/Cl	1.13	1.57	1.56	0.32	2.08	3.95	2.32
Cl/Br	81.0	76.7	23.3	28.2	30.1	33.5	24.8
Selwyn Section	Yes	No	No	No	No	No	No
Analysis	As is	As is	As is	Brush	As is	Tailings	As is
Sol	161	165	181	169	270	230	168

Notes: Major elements in weight %; trace elements in ppm.

Abbreviations: FeO_T – total iron as FeO; CIA = 100*[Al₂O₃/(Al₂O₃+CaO+Na₂O+K₂O)] in mole fractions. No correction was made for chemical constituents (sulfates, carbonates, phosphates) and so CIA are minimum values.

Table S2. continued.

	Nastapoka	Brock_Inlier	Persillon	Mavor	Cumberland Brush
SiO ₂	44.6	43.6	40.4	25.9	46.8
TiO ₂	0.94	0.93	0.85	0.45	0.91
Al ₂ O ₃	8.77	8.88	7.90	5.13	9.33
FeO _T	20.4	20.1	19.1	11.9	19.8
Cr ₂ O ₃	0.43	0.43	0.36	0.19	0.42
MnO	0.20	0.29	0.22	0.19	0.27
MgO	8.83	8.77	8.14	5.87	9.15
CaO	5.36	6.01	7.75	18.4	5.44
Na ₂ O	2.64	2.49	2.47	1.92	3.14
K ₂ O	0.61	0.54	0.53	0.25	0.66
P ₂ O ₅	1.12	1.06	0.99	0.72	0.92
SO ₃	4.00	5.97	9.71	28.0	1.57
Cl	1.93	1.19	1.44	0.97	1.33
CIA	37.3	36.3	29.7	12.2	37.2
CaO/Al ₂ O ₃	0.61	0.68	0.98	3.59	0.58
SiO ₂ /Al ₂ O ₃	5.08	4.90	5.11	5.06	5.02
Al ₂ O ₃ /TiO ₂	9.33	9.55	9.29	11.40	10.25
FeO _T /MgO	2.31	2.29	2.34	2.02	2.17
FeO _T /MnO	101.9	69.2	86.7	62.4	73.4
K ₂ O/Al ₂ O ₃	0.070	0.061	0.067	0.049	0.071
K ₂ O/Na ₂ O	0.23	0.22	0.21	0.13	0.21
Cr	2951	2924	2472	1267	2893
Ni	668	855	773	282	698
Zn	753	843	621	306	776
Ge	78	99	73	49	90
Br	197	444	100	137	122
Cr/Ni	4.42	3.42	3.20	4.49	4.14
Cr/Zn	3.92	3.47	3.98	4.14	3.73
Zn/Ni	1.13	0.99	0.80	1.09	1.11
S/Cl	0.83	2.01	2.70	11.56	0.47
Cl/Br	98.0	26.8	144.0	70.8	109.0
Selwyn Section	Yes	No	Yes	Yes	No
Analysis	As is	As is	As is	Vein-rich	Brush
Sol	158	169	154	158	291

Notes: Major elements in weight %; trace elements in ppm.

Abbreviations: FeO_T – total iron as FeO; CIA = 100*[Al₂O₃/(Al₂O₃+CaO+Na₂O+K₂O)] in mole fractions.

No correction was made for chemical constituents (sulfates, carbonates, phosphates) and so CIA are minimum values.

Table S3. APXS analyses of the Gillespie Lake, Point Lake and Shaler members listed in approximate stratigraphic order from the base.

	Gillespie Lake member	Point Lake member		Shaler member					
	Gillespie	Bell Island_9	Dismal Lake	Rocknest 3*	Howells	Aillik_RP	Egalulik	Bathurst 1*	Bathurst 2*
SiO ₂	45.6	42.9	49.0	46.0	44.6	42.2	42.0	43.7	43.9
TiO ₂	1.12	0.83	0.77	0.96	0.89	0.75	0.80	1.11	1.04
Al ₂ O ₃	9.11	9.03	11.6	10.5	9.62	8.44	8.75	7.9	8.03
FeO _T	19.5	18.0	14.7	18.4	18.5	20.6	20.7	21.9	20.8
Cr ₂ O ₃	0.52	0.48	0.37	0.25	0.59	0.76	0.66	0.41	0.35
MnO	0.32	0.46	0.30	0.45	0.37	0.36	0.35	0.78	0.43
MgO	9.18	8.17	6.3	5.33	7.72	8.71	8.24	8.60	8.78
CaO	6.45	6.81	6.23	6.06	6.48	7.03	6.53	6.30	6.43
Na ₂ O	2.58	2.98	4.36	4.02	3.22	2.86	2.95	2.24	2.14
K ₂ O	0.51	1.02	1.64	1.86	1.20	0.46	0.79	2.18	2.88
P ₂ O ₅	0.88	0.96	0.9	1.08	0.76	0.73	0.8	0.83	0.89
SO ₃	2.88	7.07	2.67	4.05	5.06	5.82	6.06	3.08	3.30
Cl	1.10	1.18	0.93	0.88	0.82	1.12	1.15	0.74	0.81
CIA	35.5	32.9	36.5	34.9	34.4	31.9	33.2	31.1	30.5
SiO ₂ /Al ₂ O ₃	5.01	4.75	4.21	4.37	4.64	5.00	4.80	5.53	5.47
Al ₂ O ₃ /TiO ₂	8.13	10.88	15.10	10.95	10.81	11.25	10.94	7.12	7.72
FeO _T /MgO	2.12	2.20	2.33	3.45	2.40	2.36	2.51	2.55	2.37
FeO _T /MnO	60.9	39.1	49.0	40.8	50.0	57.2	59.1	28.1	48.4
K ₂ O/Al ₂ O ₃	0.056	0.113	0.141	0.177	0.125	0.055	0.090	0.276	0.359
K ₂ O/Na ₂ O	0.20	0.34	0.38	0.46	0.37	0.16	0.27	0.97	1.35
CaO/Al ₂ O ₃	0.71	0.75	0.54	0.58	0.67	0.83	0.75	0.80	0.80
Cr	3545	3319	2525	1686	4060	5200	4487	2775	2403
Ni	320	290	212	364	280	234	279	395	321
Zn	591	631	480	888	814	984	967	1332	1210
Ge	39	30	31	102	60	51	54	81	46
Br	93	89	104	62	47	408	169	14	39
Cr/Ni	11.08	11.44	11.91	4.63	14.50	22.22	16.08	7.03	7.49
Cr/Zn	6.00	5.26	5.26	1.90	4.99	5.28	4.64	2.08	1.99
Zn/Ni	1.85	2.18	2.26	2.44	2.91	4.21	3.47	3.37	3.77
S/Cl	1.05	2.40	1.15	1.84	2.47	2.08	2.11	1.67	1.63
Cl/Br	118.3	132.6	89.4	141.9	174.5	27.5	68.0	528.6	207.7
Selwyn Section	No	No	No	No	No	No	No	No	No
Analysis	As is	As is	As is	As is	As is	As is	As is	As is	As is
Sol	132	117	305	102	323	322	323	54	54

Notes: Major elements in weight %; trace elements in ppm.

Abbreviations: FeO_T – total iron as FeO; CIA = 100*[Al₂O₃/(Al₂O₃+CaO+Na₂O+K₂O)] in mole fractions.

No correction was made for chemical constituents (sulfates, carbonates, phosphates) and so CIA are minimum values.

*- Rocknest3, Bathurst1 and Bathurst2 from ref. 30.

Table S4. APXS analyses of diagenetic features.

	Dike	Sayunei Raster Analysis					McGrath Raster Analysis				
	Snake_River	Center	A	B	C	D	R1	R2	R2	R4	R5
SiO ₂	42.3	38.4	36.9	37.5	43.9	41.9	43.2	43.7	43.2	42.7	42.6
TiO ₂	1.00	0.83	0.68	0.87	0.87	0.85	1.02	0.85	0.90	0.94	0.87
Al ₂ O ₃	7.52	7.45	7.44	7.78	9.43	7.77	8.35	6.70	8.56	8.16	7.24
FeO _T	21.7	17.7	17.1	17.4	18.6	21.7	20.5	23.6	19.5	20.2	22.6
Cr ₂ O ₃	0.76	0.38	0.34	0.42	0.47	0.26	0.33	0.34	0.43	0.42	0.37
MnO	0.34	0.24	0.23	0.27	0.35	0.32	0.26	0.35	0.28	0.28	0.33
MgO	8.88	8.04	9.04	8.61	8.81	9.78	8.45	10.36	8.56	8.89	9.91
CaO	6.91	9.51	9.39	9.11	6.01	5.19	5.98	4.35	6.63	6.39	5.00
Na ₂ O	2.00	2.31	2.41	2.55	2.89	2.47	2.34	2.04	2.61	2.54	2.30
K ₂ O	0.42	0.35	0.43	0.49	0.76	0.43	0.60	0.30	0.50	0.43	0.36
P ₂ O ₅	0.79	0.89	0.94	0.84	1.02	0.96	0.73	0.66	0.90	0.96	0.86
SO ₃	5.58	12.5	13.5	12.5	5.16	6.60	6.79	4.93	6.24	6.56	5.83
Cl	1.50	1.24	1.44	1.44	1.32	1.60	1.18	1.60	1.20	1.28	1.49
CIA	31.6	25.8	25.7	26.8	36.4	35.7	35.2	36.6	33.6	33.4	35.3
SiO ₂ /Al ₂ O ₃	5.63	5.16	4.96	4.82	4.66	5.39	5.18	6.52	5.04	5.23	5.88
Al ₂ O ₃ /TiO ₂	7.52	8.98	10.94	8.94	10.84	9.14	8.19	7.88	9.51	8.68	8.32
FeO _T /MgO	2.44	2.20	1.89	2.02	2.11	2.22	2.43	2.27	2.28	2.27	2.28
FeO _T /MnO	63.7	73.6	74.4	64.4	53.2	67.8	78.9	67.3	69.6	72.1	68.6
K ₂ O/Al ₂ O ₃	0.056	0.047	0.058	0.063	0.081	0.055	0.072	0.045	0.058	0.053	0.050
K ₂ O/Na ₂ O	0.21	0.15	0.18	0.19	0.26	0.17	0.26	0.15	0.19	0.17	0.16
CaO/Al ₂ O ₃	0.92	1.28	1.26	1.17	0.64	0.67	0.72	0.65	0.77	0.78	0.69
Cr	5170	2617	2294	2875	3203	1800	2140	2311	2972	2858	2550
Ni	175	618	654	687	580	921	554	712	710	582	745
Zn	819	602	642	621	770	824	728	893	777	753	815
Ge	0	84	93	32	47	121	70	101	55	98	122
Br	139	160	193	135	172	164	322	569	399	481	517
Cr/Ni	29.54	4.23	3.51	4.18	5.52	1.95	3.86	3.25	4.19	4.91	3.42
Cr/Zn	6.31	4.35	3.57	4.63	4.16	2.18	2.94	2.59	3.82	3.80	3.13
Zn/Ni	4.68	0.97	0.98	0.90	1.33	0.89	1.31	1.25	1.09	1.29	1.09
S/Cl	1.49	4.04	3.75	3.47	1.57	1.65	2.30	1.23	2.08	2.05	1.57
Cl/Br	107.9	77.5	74.6	106.7	76.7	97.6	36.6	28.1	30.1	26.6	28.8
Selwyn Section	Yes	No	No	No	No	No	No	No	No	No	No
Analysis	As is	As is	As is	As is	As is	As is	As is	As is	As is	As is	As is
Sol	149	165	165	165	165	165	270	270	270	270	270

Notes: Major elements in weight %; trace elements in ppm.

Abbreviations: FeO_T – total iron as FeO; CIA = 100*[Al₂O₃/(Al₂O₃+CaO+Na₂O+K₂O)] in mole fractions.

No correction was made for chemical constituents (sulfates, carbonates, phosphates) and so CIA are minimum values.

Table S5. Analytical errors for reported analyses.

Sol	Sample	Na ₂ O	MgO	Al ₂ O ₃	SiO ₂	P ₂ O ₅	SO ₃	Cl	K ₂ O	CaO	TiO ₂	Cr ₂ O ₃	MnO	FeO	Ni	Zn	Br
54	Bathurst1	0.27	0.33	0.37	0.58	0.07	0.11	0.03	0.04	0.08	0.04	0.03	0.03	0.15	38	38	8
54	Bathurst2	0.31	0.35	0.38	0.57	0.08	0.11	0.03	0.05	0.08	0.04	0.03	0.02	0.13	32	32	10
102	Rocknest3_rock	0.45	0.52	0.58	0.77	0.15	0.16	0.04	0.05	0.09	0.04	0.03	0.03	0.13	37	30	10
117	BellIsland	0.14	0.17	0.16	0.57	0.05	0.16	0.04	0.03	0.09	0.05	0.03	0.02	0.15	33	28	8
129	Costello	0.58	0.59	0.71	1.03	0.32	0.25	0.06	0.03	0.09	0.09	0.03	0.03	0.11	35	24	9
129	Flaherty	0.05	0.09	0.09	0.32	0.02	0.06	0.01	0.01	0.04	0.01	0.01	0.01	0.09	11	10	4
132	Gillespie	0.32	0.38	0.43	0.63	0.09	0.11	0.04	0.02	0.07	0.04	0.03	0.02	0.12	32	23	8
149	Snake_River	0.39	0.38	0.31	0.71	0.16	0.31	0.10	0.05	0.16	0.17	0.07	0.06	0.23	87	70	27
149	Ekwir1	0.05	0.09	0.09	0.33	0.02	0.06	0.02	0.01	0.03	0.01	0.01	0.01	0.09	11	9	4
150	Grit	0.16	0.20	0.18	0.59	0.06	0.17	0.05	0.02	0.10	0.05	0.03	0.02	0.18	50	39	16
150	Ekwir1_Brush	0.05	0.10	0.09	0.35	0.02	0.03	0.02	0.01	0.03	0.01	0.01	0.01	0.09	10	9	4
154	Persillon	0.06	0.09	0.09	0.34	0.02	0.10	0.02	0.01	0.05	0.01	0.01	0.01	0.09	17	10	3
158	Mavor	0.15	0.17	0.14	0.42	0.08	0.46	0.05	0.02	0.21	0.04	0.03	0.02	0.14	43	28	13
158	Nastapoka	0.05	0.09	0.09	0.35	0.02	0.05	0.02	0.01	0.03	0.02	0.01	0.01	0.09	13	9	4
161	Bonnet_Plume	0.23	0.25	0.22	0.61	0.08	0.19	0.07	0.03	0.11	0.05	0.04	0.03	0.18	71	46	16
161	HudsonBay	0.27	0.26	0.24	0.57	0.10	0.20	0.06	0.03	0.10	0.11	0.04	0.03	0.17	60	41	17
161	Yukon	0.07	0.10	0.12	0.41	0.02	0.09	0.02	0.01	0.05	0.02	0.01	0.01	0.09	16	12	4
162	HayCreek	0.18	0.22	0.21	0.64	0.07	0.20	0.06	0.03	0.10	0.07	0.03	0.03	0.20	57	43	13
165	Sayunei_A	0.19	0.27	0.22	0.68	0.08	0.37	0.08	0.03	0.17	0.05	0.04	0.03	0.21	74	51	19
165	Sayunei_B	0.22	0.28	0.24	0.71	0.08	0.37	0.08	0.04	0.18	0.06	0.05	0.03	0.22	82	54	19
165	Sayunei_C	0.25	0.32	0.29	0.91	0.10	0.26	0.09	0.05	0.16	0.11	0.06	0.04	0.25	97	69	23
165	Sayunei_D	0.23	0.30	0.25	0.77	0.08	0.26	0.09	0.04	0.13	0.06	0.04	0.04	0.25	95	61	20
165	Sayunei	0.05	0.08	0.07	0.22	0.02	0.10	0.02	0.01	0.05	0.01	0.01	0.01	0.05	15	10	4
168	Drill_RP	0.33	0.33	0.35	0.61	0.12	0.25	0.06	0.03	0.11	0.05	0.04	0.03	0.17	61	41	21
169	BrockInlier	0.19	0.23	0.22	0.65	0.07	0.19	0.06	0.03	0.11	0.05	0.03	0.03	0.19	66	43	21
169	Wernecke_Brushed	0.06	0.10	0.10	0.39	0.02	0.02	0.02	0.01	0.03	0.01	0.01	0.01	0.10	15	11	5
181	Divot2	0.08	0.12	0.11	0.40	0.02	0.06	0.02	0.01	0.05	0.02	0.01	0.01	0.11	22	15	7
230	DrillHoleR4	0.26	0.28	0.28	0.69	0.08	0.21	0.05	0.04	0.14	0.06	0.04	0.03	0.21	76	52	26
270	MacGrath_R1	0.37	0.44	0.49	0.71	0.11	0.21	0.05	0.03	0.09	0.05	0.03	0.03	0.16	54	37	16
270	MacGrath_R2	0.27	0.33	0.37	0.52	0.07	0.13	0.05	0.02	0.07	0.04	0.03	0.02	0.13	49	34	16
270	MacGrath_R3	0.24	0.29	0.33	0.56	0.07	0.17	0.05	0.02	0.09	0.05	0.03	0.02	0.16	51	34	18
270	MacGrath_R4	0.13	0.17	0.15	0.49	0.05	0.15	0.04	0.02	0.08	0.04	0.02	0.02	0.15	39	29	14
270	MacGrath_R5	0.09	0.13	0.14	0.28	0.02	0.06	0.02	0.01	0.03	0.01	0.01	0.01	0.09	17	12	6
291	Cumberland_Brush	0.06	0.10	0.10	0.38	0.02	0.03	0.02	0.01	0.03	0.01	0.01	0.01	0.09	14	10	4
305	DismalLake	0.08	0.08	0.12	0.38	0.02	0.04	0.02	0.02	0.04	0.01	0.01	0.01	0.08	12	10	3
322	Aillik_RP_overnight	0.06	0.09	0.09	0.34	0.02	0.06	0.02	0.01	0.04	0.01	0.01	0.01	0.09	10	12	5
323	Howells	0.13	0.16	0.17	0.57	0.04	0.13	0.03	0.03	0.08	0.03	0.03	0.02	0.15	31	30	7
323	Eqalulik	0.06	0.09	0.09	0.33	0.01	0.06	0.01	0.01	0.04	0.01	0.01	0.01	0.09	9	10	3

ChemCam Methods: ChemCam LIBS data were taken by obtaining a spectrum from each of 30 laser shots on each observation point. Each target was interrogated with between 5 and 25 observation points arranged in a line or in a rectangular grid covering the object of interest. For the purposes of this work, for each of the observation points, the first five spectra were discarded to avoid contamination by surficial dust. The data were preprocessed as described in *Wiens et al. (65)*. Briefly, the remaining 25 active spectra from each observation point are averaged together and a set of 30 background spectra taken on the same targets without the laser are averaged and subtracted from the mean active spectra. The continuum is removed, the spectra are de-noised, and an instrument optical response correction is applied. From here, data are processed separately for the major elements, the trace elements, and for sulfur.

The major element weight fraction abundances are determined using a partial least squares (PLS) multivariate approach in which a regression model is produced correlating the LIBS spectra and the corresponding elemental compositions of a training set of reference standards (e.g. ref. 66). For this work an algorithm was used known as PLS1 in which only one element is regressed at a time. The spectral training set was taken with the ChemCam flight unit prior to delivery, and the set used in this work was slightly modified from that described in *Wiens et al. (65)* by removing several outliers for the processing of specific elements. The number of components, or latent variables, was adjusted to minimize the root mean square error product (RMSEP) determined by the cross-validations of the model. The RMSEPs of the major elements are as follows: SiO₂ – 7.3 wt %, TiO₂ – 0.6, Al₂O₃ – 3.9, FeO_T – 3.2, MgO – 4.6, CaO – 4.2, Na₂O – 0.7, K₂O – 1.0. Absolute errors of the Mars data, e.g., due to any Earth-to-Mars differences in spectra, may be different from the training set cross validation, but differences likely do not expand this error envelope. Point-to-point precision of the ChemCam LIBS data was shown in the laboratory to generally be factors of 5-20 better than the RMSEP (65).

Due to the low intensity of the sulfur emission lines in the LIBS spectrum, S abundances were determined separately. To maximize efficiency for these emission lines, the emission from all channels within a local maximum were summed and placed into the channel representing the maximum. This peak-area spectrum was then processed PLS1 against a training set containing all sulfur-bearing standards from *Wiens et al. (2013)*. RMSEPs were determined from cross-validation of the training set, as above, and indicate that S abundances are accurate to approximately $\pm 20\%$ relative for SO₃ abundances > 10% (e.g., SO₃ = 10 \pm 2 wt %).

Lithium abundances were determined using a univariate peak area linear regression approach with a training set of reference standards. The RMSEP is 36 ppm, and is calculated in the same manner as the major elements. Strontium abundances were determined from modified PLS1 models. The PLS1 method is similar to that described for the major elements but instead of using a large wavelength range, the model only inputs the wavelengths that are strongly correlated to Sr in the training set, and are known to be emissions from Sr transitions. This reduces the likelihood that Sr will be estimated solely on major element correlations. Two models were developed for Sr because the chemical matrix affected Sr to a fairly significant degree and samples with an igneous or

igneous-like suite of major elements were placed in one model and all samples, including sulfates, carbonates and Al-clays were placed in a second model. The igneous matrix model has an RMSEP of 160 ppm and the all-samples model has an RMSEP of 432 ppm. The Sr in the ChemCam analysis points that analyzed Ca-sulfate vein material were estimated using the all-samples model while points on the surrounding igneous-like matrix were estimated using the igneous matrix model. To further constrain Sr abundances in the Ca-sulfate matrix, an additional model that contains only Ca-sulfates, may be developed.

Mass Balance Calculations: We carried several mass balance calculations to better constrain the nature of the diagenetic phases and a possible meteoritic contribution to the Sheepbed member of the Yellowknife Bay formation.

Concretion compositions. We attempted to constrain the composition of the spherules, interpreted to be sedimentary concretions (2). The two drill holes at the targets John_Klein and Cumberland were selected to evaluate the composition of the spherules with Cumberland being in an area with more spherules and the target itself having a higher abundance of spherules+minibowls. There are numerous analyses at each drill site but we chose to use the drill fines, those that accumulated on the surface during the drilling process, for comparison. The drill powders actually delivered to and analyzed by CheMin and SAM would be better but at the time of writing, Curiosity was still carrying the Cumberland sample and accordingly, no APXS analysis is available. We carried out a two-step model. First, the equivalent of 5% Ca-sulfate as anhydrite was removed from the John_Klein analysis, an amount chosen to put SO₃ abundances at similar levels in both analyses and to be consistent with vein mapping in the drill hole (4). After this correction, a gain(+) /loss(-) mass balance was calculated:

$$\Delta C^j / C^i (\%) = 100 * \left[\frac{C_s^j / C_s^i}{C_p^j / C_p^i} - 1 \right] \quad (1)$$

where C is concentration in weight percent or ppm, superscripts j and i are element of interest and an “immobile” element respectively, and subscripts s and p are sample of interest (Cumberland) and reference sample (John_Klein) respectively.

Two calculations were carried out by assuming that in one case Al was “immobile” and in the other case that Ti was “immobile. Elements enriched in Cumberland by >5% in both calculations included Fe, Ca, Cl, Br, Ni and Ge. Elevated Ca is difficult to interpret given the Ca-sulfate fractures but elevated Fe, Cl, Br and Ni are consistent with small amounts of a minor mineral such as akaganeite, identified by XRD, forming the concretion cement (4). Calculations are summarized in Table S6.

Table S6. John_Klein – Cumberland gain/loss calculations.

	John_Klein Drill Fines	Anhydrite	John_Klein less 5% Anhydrite	Cumberland Drill Fines	Gain/Loss for Al immobile	Gain/Loss for Ti immobile
SiO ₂	41.0		43.2	43.0	3.7	9.9
TiO ₂	1.02		1.07	0.97	-5.6	0.0
Al ₂ O ₃	8.47		8.92	8.57	0.0	6.0
FeO _T	20.8		21.9	22.4	6.4	12.8
Cr ₂ O ₃	0.467		0.49	0.432	-8.5	-3.1
MnO	0.32		0.34	0.3	-7.3	-1.8
MgO	8.92		9.39	9.41	4.3	10.6
CaO	7.92	41.20	6.17	6.29	6.1	12.5
Na ₂ O	2.95		3.11	2.98	-0.1	5.9
K ₂ O	0.54		0.57	0.5	-8.4	-3.0
P ₂ O ₅	0.91		0.96	0.95	3.2	9.4
SO ₃	5.94	58.80	3.16	2.57	-15.3	-10.2
Cl	0.53		0.56	1.41	163.1	178.8
Ni	698		734.7	882	24.9	32.4
Zn	810		852.6	856	4.5	10.7
Ge	77		81.1	95	22.0	29.3
Br	45		47.4	115	152.7	167.8

Cements in diagenetic fractures (“raised ridges”). Raised ridges are characterized by isopachous banding along the margins of the fractures, which could be the location of cementing agents. ChemCam first identified high MgO associated with raised ridges and this was confirmed by APXS raster analysis on the target McGrath, which further indicated elevated Fe and that both Mg and Fe correlate with Cl. In order to constrain the composition of the Mg-rich phase we carried out a series of mass balance calculations using the highest and lowest APXS MgO analyses from the McGrath raster (McGrath-1 and McGrath-2). The composition of the phase was calculated by increasing the proportion of the Mg-rich phase in increments of 5% until all elements, except for Ca, S and K, were positive in the Mg-rich phase (Table S7), using the formula:

$$C_{Mg-phase} = [C_{McGrath-2} - (1-x)C_{McGrath-1}] / x \quad (2)$$

where $C_{Mg-phase}$, $C_{McGrath-1}$ and $C_{McGrath-2}$ are the concentrations of an element in the Mg-rich phase, McGrath-1 and McGrath-2 respectively and x is the proportion of the Mg-rich phase in McGrath-2. Ca and S were neglected because of the possibility of variable Ca-sulfate veining and K was neglected because its concentration is low and variable among the McGrath raster samples. The optimum point was reached when the phase constituted 20% of McGrath-2, and for these conditions, indicates a composition for the Mg-rich phase of $SiO_2 \sim 46\%$; $FeO_T \sim 36\%$; $MgO \sim 18\%$, $Cl \sim 3\%$ and $\sim 1,300-1,500$ ppm each for Ni, Zn and Br. Such a composition cannot be accommodated by any single phase identified in the drill holes by XRD (4), but perhaps consistent with a mixture of Mg-rich, Al-deficient smectitic clay (e.g., hectorite, stevensite) and Cl-bearing Fe-oxides (e.g., akaganeite).

Table S7. Mass balance calculations estimating the composition of a Mg-rich phase in raised ridges, identified by ChemCam, using analyses from McGrath APXS raster analysis.

	McGrath 1	McGrath 2	10% Phase	15% Phase	20% Phase	25% Phase
SiO ₂	43.2	43.7	48.0	46.4	45.6	45.2
TiO ₂	1.02	0.85	-0.68	-0.11	0.17	0.34
Al ₂ O ₃	8.35	6.7	-8.15	-2.65	0.10	1.75
FeO _T	20.5	23.6	50.8	40.7	35.7	32.6
Cr ₂ O ₃	0.33	0.34	0.43	0.40	0.38	0.37
MnO	0.26	0.35	1.16	0.86	0.71	0.62
MgO	8.45	10.36	27.55	21.18	18.00	16.09
CaO	5.98	4.35	-10.32	-4.89	-2.17	-0.54
Na ₂ O	2.34	2.04	-0.66	0.34	0.84	1.14
K ₂ O	0.596	0.297	-2.39	-1.40	-0.90	-0.60
P ₂ O ₅	0.73	0.66	0.03	0.26	0.38	0.45
SO ₃	6.79	4.93	-11.81	-5.61	-2.51	-0.65
Cl	1.18	1.6	5.38	3.98	3.28	2.86
Ni	554	712	2134	1607	1344	1186
Zn	728	893	2378	1828	1553	1388
Ge	70	101	380	277	225	194
Br	322	569	2792	1969	1557	1310

Meteoritic component in the Sheepbed member. Planetary soils from the Moon and Mars show evidence for meteoritic components, typically on the order of $\sim 2-3\%$ (12) and an ancient fine-grained lacustrine sedimentary rock deposited in a distal facies of an alluvial fan on Mars could also be a site where meteoritic material might accumulate. Of the elements analyzed at Yellowknife Bay, nickel is by far the most sensitive for evaluating meteoritic components and the effects of mixing a CI chondritic composition was evaluated in Fig. 4B using a simple mixing calculation of the form:

$$C_{mix} = xC_{CI} + (1-x)C_{sample}$$

Where C_{sample} , C_{CI} and C_{mix} are the concentrations of an element in the starting sample (Martian crust or Ekwir_brush), average CI chondrite and the mixture respectively and x is the proportion of CI chondrite in the mixture. Mixing components and Cr, Ni and Zn concentrations used in the calculations were:

- (1) Average Martian crust (12). Note that this estimate of the Martian crust is based in part on average Martian soils and a 2% meteoritic component is subtracted. The composition of this end member is: Cr = 2600 ppm; Zn = 320 ppm; Ni = 337 ppm.
- (2) Lower Sheepbed member sample Ekwir_brush. This sample was selected because it is the only brushed sample in the lower Sheepbed member and thus is least contaminated by surface soils and dust. The composition of this end member is: Cr = 3051 ppm; Zn = 789 ppm; Ni = 482 ppm.
- (3) Average CI chondritic meteorite was taken to represent average meteoritic material, although we recognize that different classes of meteorites could have different levels of these elements. The composition used is the average of those tabulated in *Taylor and McLennan (12)*, and the composition used was: Cr = 2653 ppm; Zn = 317 ppm; Ni = 10,900 ppm.

Thermochemical Modeling of Diagenesis at Yellowknife Bay: The Yellowknife Bay formation has undergone at least two diagenetic events associated with phyllosilicate formation and then Ca-sulfate formation (2). In this section, we demonstrate that geochemical modeling can be used to support this observation and puts constraint on the water to rock ratios as well as the newly formed alteration minerals and the water composition during the diagenesis. We use CHIM-XPT (67) for our model.

Figure S2 shows alteration minerals forming from a rock of Ekwir_Brushed APXS composition (Table S1) at different water to rock ratios. The water to rock ratio (W/R) is a measure of the amount of water that reacted with the rock, or in other words the water activity. This has to be distinguished from the amount of water that was present. This is best illustrated by the observation of low salinity (2) and thus high complementary W/R during deposition of the Yellowknife Bay formation. However, at the same time olivine remains present in at least some of the sedimentary rocks e.g. the John_Klein drill sample (4). This shows that there is unreacted rock in the system, and therefore a relatively low volume of water was present in the total volume of reacted and unreacted rock.

We consider 3 different W/R scenarios: Very high W/R (>12000), intermediate W/R (1000–300) and low W/R (<100): At very high W/R, chlorite is formed alongside hematite. Note, that any precipitate at this W/R is only present in very small abundances, because very small amounts of rock react with the water. In light of the low overall volume of water, finding such alteration products seems unlikely, because their frequent occurrence would require more water than the observations support. At intermediate W/R the situation is different, because more precipitate is formed, and in a rock of Ekwir_Brushed bulk composition dominated by Fe-smectite clay (equivalent to nontronite in our model), with up to 35% of chlorite. At low W/R chlorite becomes the dominating alteration product, accompanied by hematite, quartz and talc. Pyroxene will not form for kinetic reasons. Note that true chlorite was not identified by XRD of drill samples but there may be a chlorite-like component in the phyllosilicates (4).

The most important scenario in the case of Yellowknife Bay is probably the intermediate W/R (Fig. S1), because it supports the link between W/R and salinity of the fluid, and is consistent with the saponite-chlorite and iron oxide found by CheMin (4). In fact, the fluid in equilibrium with the alteration assemblage at a W/R of 1000 contains

